Strengths and Weaknesses of Energy-Based Scatter Estimation using three basis functions

Seyed Amir Zaman Pour[1,*], **Ahmadreza Rezaei**[1], **Floris Jansen**[2], **Kristof Baete**[2,3], **Georg Schramm**[1], **Johan Nuyts**[1]

[1] University of Leuven, Department of Imaging and Pathology, Nuclear Medicine & Molecular Imaging, Leuven, Belgium.
[2] Formerly at Department of Engineering, GE HealthCare, Waukesha, WI 53188 USA
[3] Nuclear Medicine, University Hospitals Leuven, UZ Leuven, Campus Gasthuisberg, Herestraat 49, BE-3000, Leuven, Belgium

E-mail: seyedamir.zamanpour@kuleuven.be
*Corresponding author: seyedamir.zamanpour@kuleuven.be

Abstract. Objective: Quantitative imaging in positron emission tomography (PET) requires accurate, precise, and efficient scatter correction techniques. Conventional scatter estimation typically relies on single-scatter simulation (SSS) combined with a tail-fitting strategy. However, the accuracy of tail-fitted SSS is limited, for example, by mismatches between the attenuation image and the PET emission data or by the presence of activity outside the field of view (FOV). These shortcomings can be addressed using energy-based scatter estimation (EBSE), as recently proposed by Efthimiou et al. 2022 and Hamill et al. 2024. The aim of this work is to (1) investigate the accuracy of EBSE by accounting for the line-of-response (LOR) dependence of the energy spectrum of unscattered photons, (2) improve the computational speed of EBSE through better initialization and a more efficient optimization algorithm, and (3) Validation and characterization of EBSE using a three-basis model across different object sizes and activity distributions.

Approach: The proposed improved EBSE method models the energy spectrum of scattered photons with two probability density functions (PDFs), and incorporates a position-dependent (local) energy PDF for unscattered photons. These energy PDFs form the basis of a forward model — a linear nine-parameter model and a non-linear five parameter model — used for scatter estimation based on 2D energy histograms. The performance of the EBSE was evaluated using GATE Monte Carlo simulations and a NEMA phantom acquisition on a GE SIGNA PET/MR scanner. Furthermore, we assessed the stability of EBSE across the forward model by varying the number of counts in the 2D energy histograms via data mashing.

Main results: EBSE reduced artifacts caused by out-of-FOV activity and demonstrated performance comparable to tail-fitted SSS in other regions. Incorporating a local unscattered PDF improved off-center quantification, and NEGML with improved initialization plus histogram down-sampling substantially reduced computation without compromising accuracy. Limitations were observed: the proposed basis-function model for scattered-photon energy spectra lacks full generality across attenuation and activity distributions.

Significance: This study improves the accuracy and computational efficiency

of EBSE for clinically realistic activity and attenuation conditions, while clarifying scattered basis function limitations.

Keywords: PET, scatter estimation, energy-based scatter estimation

1. Introduction

Positron emission tomography (PET) is a widely used medical imaging modality that provides insights into functional and metabolic processes within the human body.
When positrons emitted from the radiotracer annihilate with electrons, they produce two 511 keV gamma rays emitted back-to-back, which are subsequently detected in coincidence, including time-of-flight (TOF), when TOF information is available.
However, some of these gamma rays undergo Compton scattering within the patient, reducing their energy and altering their direction of travel. This scattering effect introduces image artifacts and degrades image quality when not modeled during iterative image reconstruction, underscoring the need for effective scatter correction techniques (Zaidi et al. 2004).
Single Scatter Simulation (SSS) is a widely used approach for scatter correction in PET (Ollinger 1996). This method utilizes PET emission data and an attenuation image as inputs and follows an iterative, simulation-based process consisting of multiple stages: 1) Initially, an activity image is reconstructed from the emission data, with attenuation but without scatter correction. 2) A preliminary scatter estimate is then generated using the attenuation map and the non-scatter-corrected activity image. This estimation is based on the Klein-Nishina formula, under the primary assumption that in a pair of photons, only one of the photons Compton scatters once. Subsequently, a Gaussian-filtered version of the single-scatter estimate is added to account for shape changes caused by multiple scattering, followed by scaling to the emission data outside the patient (tail-fitting) (Watson 2005). 3) The resulting scatter estimate is used to produce a scatter-corrected version of the emission image. 4) The process is then repeated, with the non-scatter-corrected image being replaced by the newly generated scatter-corrected version, and this iteration is continued until the desired result is obtained.
Despite its extensive utilization, the tail-fitted SSS approach has several limitations.

(i) It relies on an attenuation map, making it susceptible to misalignment between the attenuation map and emission data, particularly due to patient motion between CT and PET acquisitions.

(ii) The approach is not applicable when an attenuation map is unavailable or when artifacts in the attenuation image affect the scatter estimate.

(iii) For larger objects, the accuracy of scatter estimation is diminished due to limitations in the underlying assumptions. To approximate multiple scattering, the model employs sinogram-based tail fitting; however, this simplification is inherently inaccurate and lacks stability for low-count emission data, which is common in

dynamic PET or short scan durations. An alternative method, double-scatter simulation, was introduced by (Watson et al. 2018) to eliminate the need for tail fitting, though it increases simulation time.

(iv) The SSS approach does not account for scattering from activity outside the field of view (FOV).

Several research groups have investigated energy-based scatter correction methods as an alternative to the tail-fitted SSS approach. In non-energy-based techniques, the energy of incoming photons is used solely to reject low-energy photons using an energy window (e.g. 425-650 keV). In contrast, energy-based scatter estimation (EBSE) utilizes the energy of each detected photon to estimate the scatter fraction, addressing many of the limitations associated with the tail-fitted SSS. Notably, this method does not require an attenuation map, eliminating issues related to misalignment between attenuation and emission data. This also makes it suitable for joint activity and attenuation estimation, where the initial absence of the attenuation map makes application of SSS rather cumbersome (Rezaei et al. 2019).

In the early stages of research on energy-based scatter correction for PET, technological limitations imposed constraints on the scope of the investigation, with the analysis being performed on only a few energy windows (Bendriem et al. 1993; Shao et al. 1994; Grootoonk et al. 1996). More recent energy-based methods made use of the detailed energy information provided by the listmode data (Popescu et al. 2006; Efthimiou et al. 2022). The method of (Hamill et al. 2024) fits a nine-parameter forward model to the 2D energy histograms, which accounts for unscattered, single-scattered, and multi-scattered photons in the detected photon pairs.

The present independent study builds on the results of (Hamill et al. 2024) and proposes an improved EBSE method as an alternative to the tail-fitted SSS approach in PET imaging. The strengths and weaknesses of this method are identified with carefully designed simulation experiments and with a real NEMA phantom scan. Specifically, our work on EBSE includes the following novelties:

(i) An investigation of the dependence of the energy spectrum of unscattered photons (which is needed to model the 2D energy spectrum of all prompt photon pairs) on the incidence angle of the line of response (LOR) and its impact on EBSE.

(ii) An analytical derivation, which leads to the same basis functions as proposed by (Hamill et al. 2024), but provides additional insight, and may be the basis of further improvements to the scatter model.

(iii) An implementation of a faster maximum likelihood estimator using a better initialization and optimization algorithm (Section 2.4) to achieve substantially faster convergence of model fitting.

(iv) An investigation of the effect of sinogram mashing (down-sampling) on the bias and noise of the final scatter corrected image.

(v) An evaluation of EBSE on different object sizes and challenging activity distributions, designed to reveal its current strengths and weaknesses.

To assess the proposed improvements for EBSE, Monte Carlo simulations with GATE (Jan et al. 2004) and MCGPU-PET (Herraiz et al. 2024) were performed. In addition, phantom measurements acquired on the GE SIGNA PET/MR system were analyzed.

2. Methods

2.1. Theory

The proposed approach involves modeling the measured 2D energy histograms. The 2D energy histogram represents the 2D energy distribution of photon pairs detected in a given TOF bin on a given line of response (LOR). Fig. 1 (A) shows such a 2D energy histogram of GATE simulated data. Since this is a simulation, the histogram can be decomposed into unscattered, scattered and random coincidences - see Figure 1 (B-D). The total prompt coincidence count in the simulation was 7.9×10^7, resulting in an average of approximately 460 counts per 2D energy histogram when using sinogram mashing. In the following, we use the term "unscattered" photon pairs for coincidences where neither photon underwent Compton interactions within the patient.

To estimate the fractions of scattered and unscattered photon pairs, we use a model that defines basis functions corresponding to photon pairs with different scatter histories, to model the measured 2D energy histograms. One basis function represents the 2D energy distribution of unscattered photon pairs, while all other basis functions correspond to photon pairs with one or more scatter interactions. By estimating the weight of each basis function, the relative fractions of unscattered and scattered photon pairs can be determined. Since a single photon can have three scatter histories: "unscattered", "single Compton scatter," or "multi-Compton scatter", 9 basis functions are used to model the 2D energy distribution (Hamill et al. 2024). The weights of the basis functions are estimated by optimizing the Poisson log-likelihood function, subject to a non-negativity constraint.

A full energy-based scatter sinogram can be generated by applying EBSE to the measured 2D energy histograms of all TOF bins along all LORs. This scatter sinogram can then be used in the maximum likelihood expectation maximization (MLEM) activity reconstruction as the expectation of the scatter contribution.

The main processing pipeline for EBSE thus consists of the following steps:

(i) Definition of energy probability density function (PDF) of single photons.

(ii) Construction of 2D forward model basis functions for the 2D energy histogram, based on the single photon energy PDFs.

(iii) Estimation of the weights of these basis functions, which can be used to derive the scatter fraction.

Note that in contrast to SSS or double scatter simulation, EBSE only needs to be applied once before reconstruction directly using the measured data.

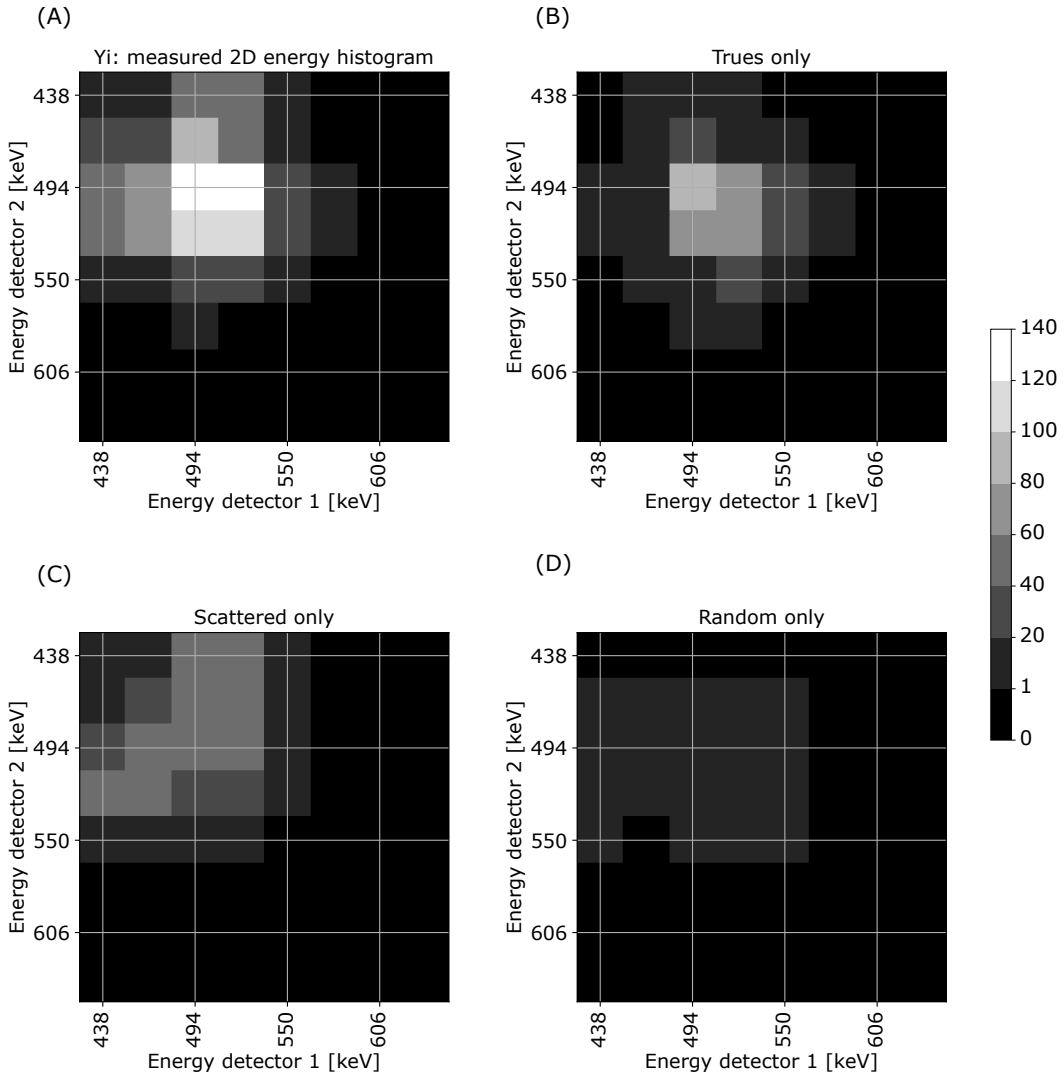

Figure 1: (A) an emission 2D energy histogram of the data collected in the down-sampled sinogram in a single TOF bin. (B) Trues coincidence 2D energy histogram corresponding to (A). (C) Scattered coincidences 2D energy histogram of (A). (D) Random coincidences 2D energy histogram of (A). The x-axis represents the energy of photons detected in detector 1, while the y-axis represents the energy of photons detected in detector 2.

2.2. Single-Photon Energy PDFs

2.2.1. Local/Global Unscattered Photons Energy PSF (P_0): To determine the energy spectrum of single unscattered photons, denoted as P_0, a common approach based on previous works on EBSE (Hamill et al. 2024) and (Efthimiou et al. 2022) is to extract the single-photon energy spectrum from a point-source measurement placed at the scanner's center. Applying this single basis function uniformly across all LORs in energy-based scatter estimation is referred to as EBSE with a "global unscattered PDF" or "global P_0". The global unscattered energy spectrum is obtained from the LORs intersecting

the point source, with these LORs being predominantly perpendicular to the detector face.

However, the energy spectrum of single unscattered photons depends on the incidence angle between the detector face and the incoming photon. In many single-photon detections, the photon deposits less than its full energy in the crystal, due to within-crystal Compton or X-ray escape. Consequently, the energy spectrum of single unscattered photons is not perfectly Gaussian, and since the energy escape depends on the incidence angle, so does the spectrum. This results in a non-Gaussian energy spectrum for single unscattered photons with an elevated lower energy tail that depends on the incidence angle - see Fig. 6. To account for this dependence, we propose to use a local incidence-angle dependent energy spectrum of unscattered single photons called "local unscattered PDF" or "local P_0". The following steps were undertaken to derive the local unscattered PDF.

(i) The incidence angles in three dimensions were computed for every LOR. Because the scanner ring is not perfectly cylindrical, the two incidence angles associated with a given LOR—one for each opposing detector—are similar but in general not identical, except at the central radial bin. Thus, each LOR is characterized by two angles, θ_1 and θ_2 (Fig. 2 A). For subsequent analyses, a single representative incidence angle was defined as the mean of the two: $\theta = (\theta_1 + \theta_2)/2$.

(ii) The mean incidence angle for each LOR was calculated and mapped back to its sinogram coordinates. The sinogram was segmented into 13 regions based on the intrinsic geometric pattern of the map (see Fig 2 B). The mean incidence angle was found to range from 0°–81.97°. In the direct (zero-obliquity) plane shown, the highest-angle segment is not visible because it occurs only in highly oblique planes.

(iii) Two approaches were used to extract the local unscattered single-photon spectrum, P_0, depending on the data source. In the GATE simulations (Section 2.6.2), the described experiment was performed and, for each of the 13 incidence-angle segments, an energy spectrum was extracted. For the GE SIGNA PET/MR acquisitions (Section 2.6.9), the simulation-style per-segment extraction was not feasible; therefore, the 13 segments were merged into three regions according to the intrinsic pattern observed in the incidence-angle sinogram (see Fig 2 C), yielding smoother and more stable estimates of the local P_0.

2.2.2. Single Compton Scatter Energy PDF (P_1 and P_2): Two basis functions are employed to characterize the PDF of scattered single photons. Under the simplifying assumption of a spatially uniform, extended activity distribution (ignoring limited-angle scattering effects), the single-scatter energy spectrum is derived from the Klein–Nishina (KN) formula in Appendix A.1, and shown as the black curve in Figure 3(A). For practical modeling within the defined region of interest (energies above 425 keV), a linear model indicated by the red dashed line was fitted. The KN differential cross-section specifies the angular probability of Compton scattering but does not account for

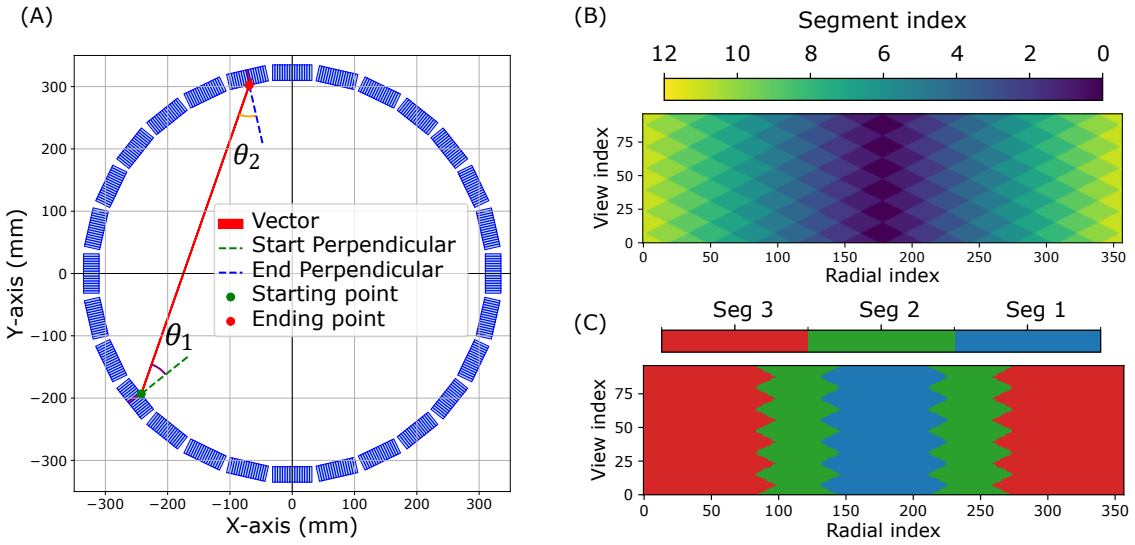

Figure 2: (A) Incidence angle visualization for one LOR in transaxial scanner view. (B) segmented version of the sinogram of incidence angles based on intrinsic patterns (B) Angle-of-incidence sinogram segmented using intrinsic geometric patterns; this segmentation was applied to all GATE simulations with local P_0. (C) In real-data acquisitions, the 13 segments were merged, based on the observed pattern, into three regions (Seg 1–3) for extracting local true-coincidence energy spectra.

attenuation along the photon paths. In Appendix A.3, the effect of uniform attenuation and the detector solid angles on the spectrum is calculated. The resulting spectrum can still be approximated well with a first order function for energies above 425 keV, but the function becomes steeper with stronger attenuation. Therefore, we model the single scatter as a weighted sum of two basis functions, P_1 and P_2. P_1 is a linear curve which is zero at $\mathrm{E_{min}}$, increases linearly to its maximum at 511 keV and then drops to zero. P_2 is also a linear curve, it becomes zero at 511 keV. P_1 determines the steepest slope, and adding a weighted version of P_2 makes it less steep. The steepness of P_1 is parametrized by $\mathrm{E_{min}}$, the intersection of the P_1 with the energy axis.

The energy spectrum of Compton-scattered photons was investigated with GATE Monte Carlo simulations of a uniform radioactive cylinder with 20 cm diameter, filled with water (see Section 2.6.3). The simulation was done for perfect energy resolution. From all LORs intersecting the object, the energy spectrum of single-Compton–scattered photons was extracted; it is shown as the green curve in Fig. 3(D). Fitting a line to this spectrum produced an $\mathrm{E_{min}}$ value of approximately 300 keV, shown as the red dotted line in Fig. 3(D). This agrees well with the calculation in appendix A.3, which produced $\mathrm{E_{min}} = 283$ keV for an attenuator thickness of 20 cm. This observation also aligns well with findings reported by (Hamill et al. 2024). Because the solid angles of the detector pair and the total attenuation associated with each LOR are different, the single-scattered photon spectrum is modeled as a weighted sum $S_1P_1 + S_1'P_2$, with

different weights for each LOR. E_{min} sets the steepness of basis function P_1, which serves as the maximum slope limit for the model. Due to the non-negativity constraints applied to the weights (S_1 and S_1'), any linear combination involving the positive-slope P_2 results in a slope shallower than P_1. Thus, the model cannot generate a spectrum steeper than the initial P_1 basis.

2.2.3. Multiple Compton Scatter Energy PDF (P_2): As shown in Appendix A.2, for energies above 425 keV, the spectrum of multi-Compton-scattered single photons can be modeled as an oblique line, which becomes zero at 511 keV (the purple dashed line in Fig. 3(A)). Thus, we can reuse P_2 and model the multiple-scattered as $S_2'P_2$. The multi-Compton scattered energy spectrum was derived by convolving the KN distribution (black curve) with itself, yielding the double-scattering spectrum (blue curve) shown in Fig. 3(A). The linear approximation $S_2'P_2$ is only valid for the energy range of interest, above 425 keV. The curves have been extended down to 0 keV purely for completeness. This result was verified with Monte Carlo simulation: the resulting multiple scatter energy spectrum from all LORs intersecting the object is shown as the orange code in Fig. 3(D).

2.2.4. The single photon energy PDF ($S_0P_0+S_1P1+S_2P_2$): From the above, it follows that the entire single photon spectrum is modeled as $S_0P_0 + S_1P_1 + S_1'P_2 + S_2'P_2 = S_0P_0 + S_1P_1 + S_2P_2$, with $S_2 = S_1' + S_2'$. The parameters S_1' and S_2' are not identifiable by fitting to the data, but their sum S_2 is, so a single photon spectrum is modeled using the three known basis functions P_0, P_1 and P_2, and fitting their weights S_0, S_1 and S_2. The analytical method for computing P_1 and P_2 is provided in Appendix A.

A Gaussian convolution is utilized to model the scanner's energy resolution, and the full width at half maximum (FWHM) of the kernel was 11.2% at 511 keV, as determined from point source measurements on the GE SIGNA PET/MR scanner. Although Gaussian smoothing does not perfectly represent detector energy resolution, the approximation was employed for simplification. The effect of the incidence angle on scattered photons is neglected, as accurately determining the angle of photon entry relative to the detector surface requires prior knowledge of both the emission and scattering locations. The resulting effective energy spectra of P_1 and P_2 are shown in Fig. 3 (C).

It turns out that our analytically derived set of basis functions is identical to that of (Hamill et al. 2024), who deduced it from Monte Carlo simulations. The interpretation of the basis functions is different. Hamill et al. derived P_2 as the large-angle scatter spectrum, whereas we obtained it from estimating the multiple-scatter spectrum. Hamill et al. obtained P_1 as the small-angle spectrum, whereas in our calculations, the single-scatter energy spectrum was estimated as a weighted sum of P_1 and P_2.

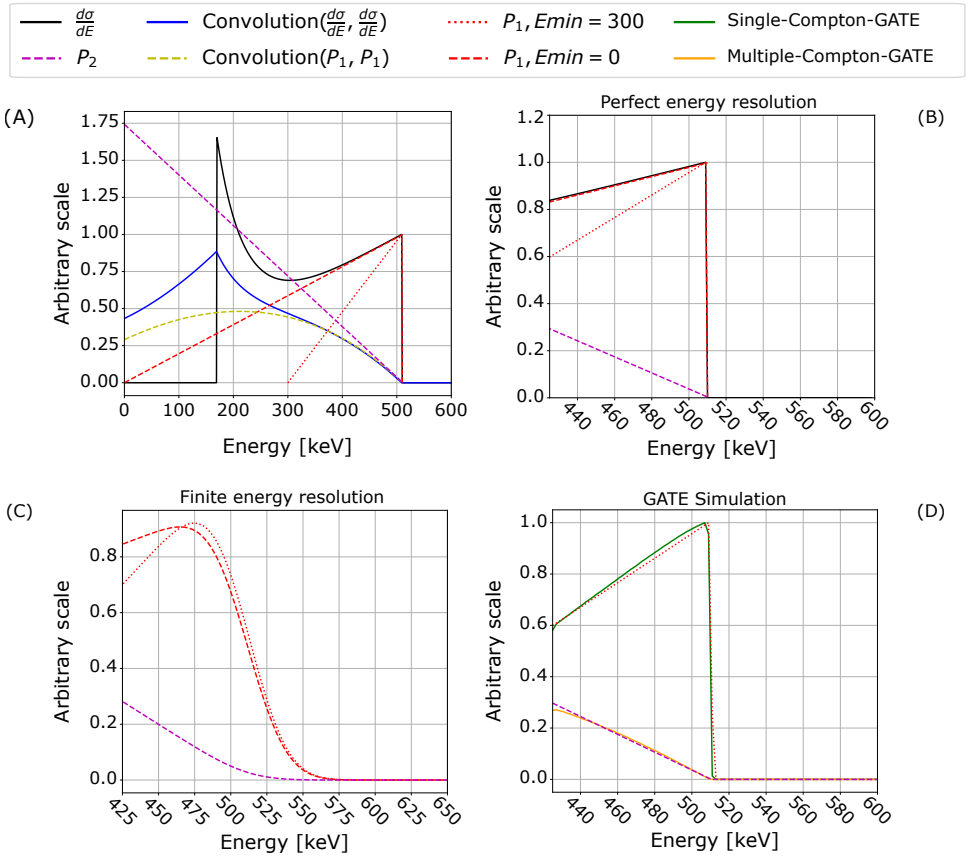

Figure 3: (A) The black curve represents the energy spectrum of single scattering, calculated using the Klein-Nishina formula. The blue curve shows the convolution of the black curve with itself, representing double scattering. The red dashed line corresponds to the model of the single Compton scattered photon above 425 keV (P_1). The yellow curve is the analytical convolution of the red dashed line with itself. The purple dashed line represents the first-order approximation of the yellow curve near 511 keV and corresponds to the model of multi-Compton scattered photons above 425 keV (P_2). Note that, with the exception of the black curve, all plotted curves are only valid models for the energy range of interest (above 425 keV); they have been extended down to 0 keV purely for completeness. (B) shows the scattered energy spectrum in the range of the energy window of the SIGNA PET/MR scanner. (C) The energy spectrum of single Compton scattering (P_1, red) and multi-Compton scattering (P_2, purple) after applying the finite energy resolution model of the scanner as Gaussian smoothing. (D) Single- and multiple-scatter energy spectra from LORs intersecting a uniform cylinder (R=100 mm) in GATE, compared with the analytical templates P_1 and P_2 using $E_{\min} = 300$ keV; spectra are normalized for shape comparison. The y-axis is the arbitrary scale, and the x-axis is energy in keV.

2.3. Forward model for the 2D joint energy joint energy distribution of photon pairs

In PET imaging, coincidences are defined by the nearly simultaneous detection of photon pairs. The 2D energy histogram, which represents the energy distribution of detected photon pairs, generally requires nine independent parameters for characterization, this is discussed below. The following definition outlines the nine-parameter forward model:

$$\begin{aligned}\hat{n}(E_i, E_j) = a_{0,0}\, P_0(E_i)P_0(E_j) + a_{0,1}\, P_0(E_i)P_1(E_j) + a_{0,2}\, P_0(E_i)P_2(E_j) \\ + a_{1,0}\, P_1(E_i)P_0(E_j) + a_{1,1}\, P_1(E_i)P_1(E_j) + a_{1,2}\, P_1(E_i)P_2(E_j) \\ + a_{2,0}\, P_2(E_i)P_0(E_j) + a_{2,1}\, P_2(E_i)P_1(E_j) + a_{2,2}\, P_2(E_i)P_2(E_j).\end{aligned} \tag{1}$$

The coefficient $a_{0,0}$ is the weight of the $P_0(E_i)P_0(E_j)$ basis function, which represents the number of photon pairs where neither of the photons underwent Compton scattering inside the patient. In contrast, the coefficients $a_{0,1}$ to $a_{2,2}$ collectively represent the number of coincidences where one or both photons experienced single or multiple Compton scattering inside the patient. The expectation of the 2D energy histogram of unscattered and scattered photon pairs, denoted as $\hat{n}(E_i, E_j)$, is computed as the weighted sum of these basis functions. Here, E_i and E_j represent the discretized detected energies of the first and second photons, respectively.
We define the expectation of the measured prompt 2D energy histogram as

$$\hat{y}(E_i, E_j) = \hat{n}(E_i, E_j) + \hat{r}(E_i, E_j) \tag{2}$$

i.e. the sum of $\hat{n}(E_i, E_j)$, along with the expectation for the 2D energy spectrum of random coincidences, $\hat{r}(E_i, E_j)$.
To compute $\hat{r}(E_i, E_j)$ for a given TOF emission data bin, the following steps are performed:

(i) The energy spectrum of photons in the delayed window is extracted. Based on this spectrum, a normalized 2D energy histogram is defined under the assumption that the energy distribution of random coincidences is LOR independent. This assumption was validated through the analysis of 2D energy histograms derived from various LORs in GATE-simulated emission data, as described in Section 2.6 (results not shown).

(ii) The normalized 2D energy histogram is then scaled according to the expected number of random coincidences in the given emission data bin, which is provided by the estimated random sinogram.

It should be noted that nine-parameter model employed in this analysis assume that the joint probability distribution factorizes as $P_1(E_i, E_j) \simeq P_1(E_i)P_1(E_j)$, effectively neglecting quantum entanglement between photon pairs. Although this approximation is known to break down due to polarization correlations in the annihilation process, such effects are negligible within the energy range considered in this study (Dikaios et al. 2006).

2.4. Optimization of model parameters

The forward-model coefficients are estimated by fitting to the measured 2D energy histogram. Maximization of the Poisson likelihood is performed with the NEGML algorithm (Van Slambrouck et al. 2014) subject to a non-negativity constraint, as it is known to accelerate convergence. This constraint enforces physical plausibility. NEGML is used here as an established ML optimizer; its performance characteristics have been evaluated previously (Van Slambrouck et al. 2014).

The efficiency of the NEGML algorithm is influenced by the number of parameters updated in each iteration. For instance, simultaneously updating all nine parameters per iteration results in a convergence rate similar to that of conventional maximum likelihood expectation maximization (MLEM). However, updating the parameters sequentially, one at a time as done in NEGML, leads to a faster convergence rate compared to standard MLEM (Van Slambrouck et al. 2014). The coefficients are estimated using the adapted version of the NEGML approach

$$\Theta_k^{(n+1)} = \Theta_k^{(n)} + \frac{\sum_{i,j} c_{i,j,k} \frac{y(E_i,E_j)-\hat{y}(E_i,E_j)}{\hat{y}(E_i,E_j)}}{\sum_{i,j} \frac{c_{i,j,k}^2}{\hat{y}(E_i,E_j)}}. \tag{3}$$

where $y(E_i, E_j)$ is the measured 2D joint energy histogram, Θ_k are the coefficients for the nine-parameter models and $c_{i,j,k}$ is $\frac{\partial \hat{n}(i,j)}{\partial \Theta_k}$.

To accelerate scatter estimation, a weighted least squares estimate was used to initialize the coefficients prior to applying NEGML. Marginal spectra $y_1(E)$ and $y_2(E)$ are obtained by summing over the other energy dimension in $y(E_i, E_j)$, yielding two 1D prompt spectra corresponding to detector 1 and detector 2. The same approach is used to compute $\hat{r}_1(E)$ and $\hat{r}_2(E)$ from $\hat{r}(E_i, E_j)$. The observed 1D prompt spectra are modeled as a linear combination of the basis functions P_0, P_1, and P_2. Given the system matrix $A = [P_1(E), P_2(E), P_3(E)]$, where $P_1(E), P_2(E), P_3(E)$ represent the PDFs, the estimation problem is formulated as:

$$\hat{y}_l(E) = Ap + \hat{r}_l(E), \quad l = 1, 2 \tag{4}$$

where p is the vector of unknown scaling factors, and l represents the index of the first or second dimension. To solve for p, we minimize the weighted least squares cost function:

$$L(p) = (y_l(E) - (Ap + \hat{r}_l(E)))^T C_{y_l}^{-1} (y_l - (Ap + \hat{r}_l(E))) \tag{5}$$

where C_{y_l} represents the covariance matrix of the measured spectrum and accounts for statistical noise. Since photon detection follows a Poisson process, the covariance matrix is assumed to be diagonal, and an initial approximation is obtained using a Gaussian smoothed (kernel size FWHM = 3 [unit is energy bin width]) estimate of the 1D marginal prompt energy spectra. The parameter estimation is refined iteratively by updating C_{y_l} based on the estimated spectrum and solving the weighted least squares. Our observations showed that after two iterations, there is almost no change in the estimated parameters. To ensure physical validity, the estimated parameters are constrained to be non-negative. This approach provides a computationally efficient and statistically robust initialization.

2.5. Sinogram downsampling (mashing)

Sinogram down-sampling was performed by merging detectors in the axial and transaxial directions, a technique known as mashing. However, this process was not applied in the TOF direction. The primary objective of mashing is to increase the number of counts per 2D energy histogram, thereby reducing statistical noise.

The mashing factor (MF) is defined based on the degree of detector merging. For instance, MF = [16,9] indicates that counts from 16 detectors in the transaxial direction and 9 detectors in the axial direction are merged. As a result, the TOF sinogram size of the GE SIGNA PET/MR scanner is reduced from (357, 224, 1981, 27) to (25, 14, 25, 27) radial, angular, planar and TOF bins, respectively.

Because scatter is estimated on a down-sampled ("mashed") sinogram, we must carry the block-pattern sensitivity through the up-sampling. The procedure is: 1. Down-sample sensitivity: the native-resolution sensitivity sinogram ϵ_g is binned into the same coarse grid as the mashed sinogram, yielding ϵ_m. 2. Normalize: divide the down-sampled scatter estimate S_m by ϵ_m to remove sensitivity weighting. 3. Upsample: expand the unweighted coarse scatter back to full resolution, distributing each S_g over its constituent fine LORs proportionally. 4. Re-apply sensitivity: multiply the up-sampled scatter S_g by the native-resolution sensitivity ϵ_g to restore the block-pattern incidence-angle effects in the final scatter sinogram.

2.6. Experiments

All experimental setups used in this study are described in this section. Two types of experiments were conducted: (i) GATE/MCGPU-based Monte Carlo simulations and (ii) GE SIGNA PET/MR acquisitions.

For image reconstruction, TOF information was modeled using a Gaussian kernel with 380 ps FWHM, equivalent to 5.7 cm along the LOR. Reconstruction used a listmode Ordered Subset MLEM (OSEM) algorithm with a voxel matrix of 240 × 240 × 101, an isotropic voxel size of 2.5 mm, 20 subsets, and 5 iterations were used for the GATE simulated data, and the measured NEMA data. Spatial resolution modeling used a narrow tube-of-response with a width-to-pixel-size ratio of 0.5 to limit cross-talk between adjacent LORs, convolved with a Gaussian kernel of 4.5 mm FWHM.

2.6.1. GATE simulation experiments: The GATE Monte Carlo simulations were performed using GATE v9.2, Geant4 11.0.3, and ROOT 6.24/06 on the Ubuntu 20.04.06 LTS operating system. The PET geometry of the SIGNA PET/MR scanner was implemented in GATE as a system consisting of 28 detector modules arranged in a polygon, in accordance with the specifications reported by (Levin et al. 2016). Each module contained a matrix of LYSO crystals, 45 in axial and 16 in transaxial direction. To accurately describe photon interactions within the detector, the Penelope physics list in GATE was used, enabling the modeling of photoelectric absorption, Compton scattering, and Rayleigh scattering in the detectors and objects. As incoming photons

interacted within the detector, their energy could be scattered or absorbed in adjacent crystals; the detection position was therefore determined using a weighted positioning derived from the deposited energy in each detector. Finite energy and time resolutions were modeled by applying Gaussian blurring to the (exact) deposited energies and detection times. Detections were accepted when the energy was within a window of 425-650 keV. Coincidence events were computed using the *takeAllGoods* policy, in which every photon detected within a coincidence window is paired with all others. As a result, events with more than two detected photons naturally give rise to multi-coincidences. To estimate the contribution of random coincidences, a delayed coincidence window with the same temporal width as the prompt window was employed, shifted by 50 ns. To reduce simulation complexity, several effects were excluded, including the intrinsic activity of ^{176}Lu in LYSO crystals, pile-up processing, attenuating media between the scanner bore and the crystal front face, optical processes (e.g., SiPM implementation and light transport), and electronic noise. For computational efficiency, detailed annihilation modeling was not included; instead, activity was represented by the emission of two gamma photons at 511 keV isotropically emitted back-to-back.

2.6.2. Computing global and local P_0 in GATE acquisition : Global and local unscattered single-photon energy spectra (P_0) were obtained from two dedicated simulations; the experimental setups were described below. These spectra were subsequently used in the EBSE evaluation on the GATE acquisitions.

(i) Global P_0 : A point source (radius 1.5 mm; activity 5 kBq) was simulated in vacuum in GATE. The source emitted back-to-back 511 keV photons and was positioned at the scanner isocenter. Because the source was not positron, no attenuating medium was required for annihilation. The unscattered single-photon energy spectrum (global P_0) was extracted from all detected true coincidences over a 20-minute acquisition, yielding 8.2×10^6 coincidences.

(ii) Local P_0: The angle-dependent unscattered spectrum setup was described in Section 2.2.1. The entire field of view was filled by a uniform cylindrical source (radius 299.5 mm; height 250 mm) at a concentration of 5 Bq/mL, simulated in vacuum with back-to-back 511 keV emission and no activity decay. In the absence of an attenuating medium, only true and random coincidences were present; the local unscattered spectrum (local P_0) was computed from all non-random (true) coincidences for each segment of sinogram shown in Fig 2(B). The simulation produced 2.4×10^9 coincidences.

2.6.3. Uniform cylinder simulation to fit $E_{\min}$: The experimental setup that was used to extract the single- and multiple-scatter energy spectra shown in Fig. 3(D) in orange and green (Section 2.2.2) consisted of a uniform water cylinder (radius 100 mm, height 250 mm) filled with activity at 100 Bq/mL. Simulations were performed with ideal (perfect) energy resolution and without radioactive decay modeling. A total of 5.1×10^8

coincidences are recorded.

2.6.4. Custom elliptical phantom simulation: A custom elliptical phantom, shown in Figure 4 (A), was defined within the GATE software. The phantom measured 460 mm in the axial direction, with a cross-sectional size of 500 mm x 300 mm. It contained nine spheres, each 37 mm in diameter, arranged in the XZ plane, shown as blue solid lines in Figure 4 (A). Additionally, a larger sphere (96 mm in diameter) was placed outside the FOV, represented by a dashed red circle in Figure 4 (A), to simulate activity in the bladder outside the axial FOV. The phantom was filled with water. The background activity concentration was 0.25 kBq/ml, while the nine spheres within the FOV were filled with 2.5 kBq/ml. The larger sphere outside the FOV had a concentration of 6.25 kBq/ml. The GATE simulation of the elliptical phantom generated around 7.9×10^7 prompt coincidences during a 15-minute PET acquisition. This experiment was repeated seven times for noise recognition. The simulations assumed constant activity; no radioactive decay modeling was applied during acquisition.

A key advantage of the GATE simulation was its ability to categorize each detected photon as either scattered (in the object) or unscattered. This classification was essential, as it enabled the precise reconstruction of unscattered coincidences only, providing a reliable ground truth reconstruction, shown in Figure 4 (B). To facilitate a comprehensive comparison between the ground truth and the energy-based scatter-corrected results, the nine sphere boundaries were precisely segmented in the activity images using the geometry map. Due to symmetry between the off-center hot regions, their average was computed for analysis. Additionally, the averages of four spherical segments from three distinct background locations were calculated. The background regions of interest (ROIs) were labeled with blue indices (A, B, and C), while the hot ROIs were denoted by red indices (1–6), as shown in Figure 4 (B). Notably, background ROI C and hot ROIs 5 and 6 were positioned near regions of activity outside the FOV. To quantify the differences, the relative error was computed for each segment using equation (6).

$$\text{Relative error of ROI mean} = \frac{\text{ROI}_{\text{mean EBSE}} - \text{ROI}_{\text{mean GT}}}{\text{ROI}_{\text{mean GT}}}. \tag{6}$$

The ROIs are shown in figure 4(b). $\text{ROI}_{\text{mean EBSE}}$ and $\text{ROI}_{\text{mean GT}}$ denote the mean activity values measured in the specified ROI for the energy-based scatter-estimation image and the ground-truth image, respectively.

2.6.5. Uniform cylinder simulation : Two uniform water-filled cylinders were simulated at the center of the scanner: (A) a cylinder with a radius of 100 mm, a height of 200 mm, and an activity concentration of 1 kBq/mL, resulting in a total of 1.70×10^8 counts; and (B) a cylinder with a radius of 210 mm, a height of 250 mm, and an activity concentration of 0.01 kBq/mL, with a total count of 2.13×10^8. Both simulations assumed constant activity; no radioactive decay modeling was applied during acquisition.

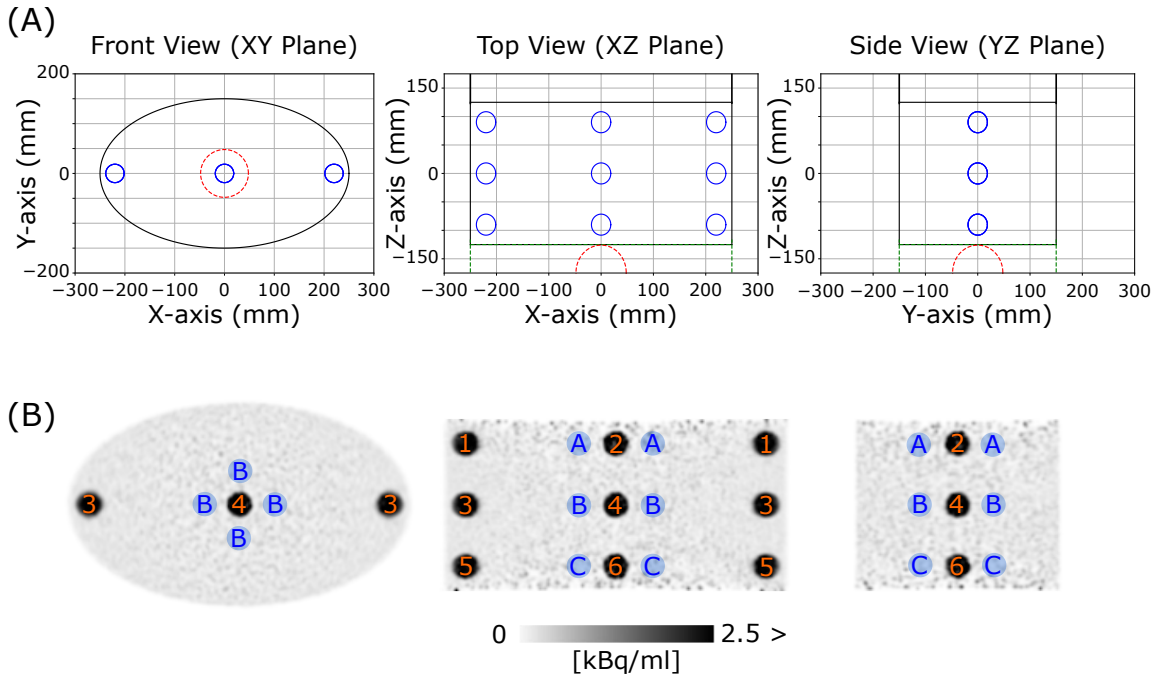

Figure 4: (A): The elliptical phantom geometry used in the GATE simulation is shown in three different plane views. Hot regions within the FOV are depicted in blue, while the red dashed line represents the hot region outside the FOV. The XY plane corresponds to the transaxial view, where the detectors are arranged in a ring, and the Z-axis represents the axial direction. (B) Activity ground truth MLEM reconstruction image of unscattered and non-random coincidences with isotropic Gaussian post-smoothing (FWHM = 2 pixels). The numbers denote the hot regions, while the blue-letter ROI corresponds to the background.

2.6.6. NEMA Phantom with activity out-of-FOV simulation: The NEMA phantom was implemented in GATE according to the geometric specifications described in section 2.6.10. The configuration shown in Fig. 15(C) was simulated with hot spheres at an activity concentration of 16 kBq/mL, a background activity concentration of 4 kBq/mL, and an out-of-FOV syringe at 800 kBq/mL in 100 ml (radius 16.3 mm and height 119 mm). The total number of prompt events was 2.77×10^8, with a corresponding random fraction of 49.2%. No radioactive decay modeling was applied during acquisition.

2.6.7. ^{18}F*-FE-PE2I and* ^{18}F*-SynVesT-1 simulation :* The performance of the proposed EBSE approach under more realistic activity distributions that deviate substantially from uniformity is evaluated. The ^{18}F-FE-PE2I is a dopamine transporter tracer, and ^{18}F-SynVesT-1 is a tracer for synaptic density imaging. The activity distributions and attenuation maps are shown in Figs. 12 and 13 ("True activity map" and "Attenuation map"). Both simulations assumed constant activity; no radioactive

decay modeling was applied during acquisition. The brain images were based on the Brainweb phantom (Collins et al. 1998). The total prompt counts were 2.18×10^8 for ^{18}F-FE-PE2I and 1.15×10^8 for ^{18}F-SynVesT-1.

2.6.8. High-counts ^{18}F-FE-PE2I simulation : In contrast to all other simulations, this simulation was done with MCGPU-PET (with the same setup as GATE simulation), a fast Monte Carlo GPU-based simulator (Herraiz et al. 2024). MCGPU-PET is a GPU-based tool that simulates photon interactions in the object while neglecting photon–detector interactions to accelerate computation. Because it is much faster than GATE, we use it here to obtain a very high number of counts in a reasonable amount of simulation time. Since photon-detector interactions are not modeled in MCGPU-PET, the simulated energy spectra reflect the incident photon energy distribution, excluding the detector response function. The activity map and attenuation are shown in Figures 12. The total non-random coincidences were 5.69×10^9 with a scatter fraction of 23.7%.

2.6.9. Line-source acquisition : A line-source measurement was performed to derive the local and global energy spectra of unscattered single photons. The comparison between the point-source and the low-incidence-angle local energy spectrum of unscattered photons in the GATE simulation shows negligible differences, which is geometrically consistent since, in a measurement of a point source at the center of the FOV, all LORs intersecting the activity are almost perpendicular to the detector. The global unscattered PDF was defined based on the energy spectrum at low incidence angles of the local unscattered PDF. A 30 cm long tube with an activity concentration of 9 kBq/cm was positioned at 10 o'clock in the scanner, 8 cm away from the gantry surface shown in Figure 5. Before extracting the energy spectrum for each incidence angle segment, Fig. 2(B), all LORs intersecting the bed were discarded to eliminate photons that scattered in the bed. To achieve a smoother energy spectrum curve for each segment, a down-sampling was performed based on the pattern of incidence angles shown in Fig 2(B) into three segments, Fig 2(C).

2.6.10. NEMA Phantom with activity out-of-FOV acquisition : A NEMA phantom measurement was performed on a GE SIGNA PET/MR scanner, with activity positioned outside the FOV in the axial direction, as shown in the Figure. 15 (C). These measurements were reconstructed using both an energy-based scatter correction method and a vendor-implemented, tail-fitted single-scatter simulation estimation approach. The scan was acquired using data from a single-bed position on a GE SIGNA PET/MR scanner operating in research mode. In this configuration, the system was set to provide energy information for single photons in coincidences. The research mode was configured with guidance from the vendor.
The NEMA phantom was filled with 3.67 kBq/ml of ^{18}F as the background activity. It had a cross-sectional size of 30 cm $\times$ 20 cm and contained six spheres with diameters

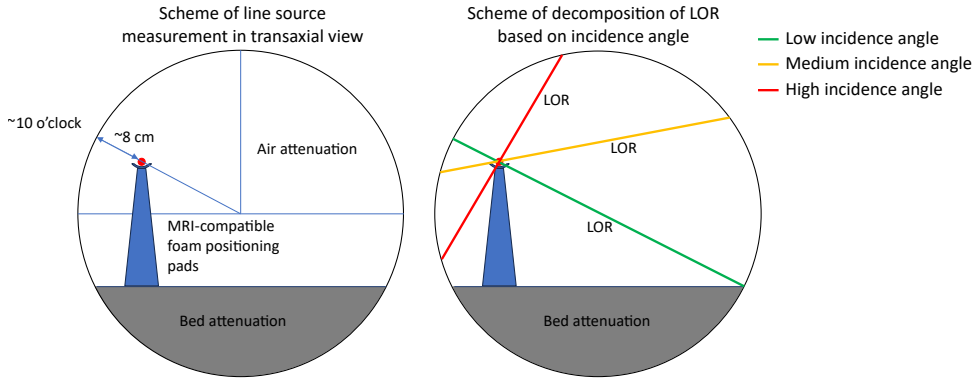

Figure 5: The schemes of line-source measurement in transaxial view. The gray part is the attenuation of bed, blue is MRI-compatible foam positioning pads to hold the line-source, and the red circle is the cross-section of the line source. The scheme of LORs with different incidence angles is denoted as lines in green, yellow, and red.

ranging from 10 to 37 mm. The largest and smallest spheres were filled with a 15.18 kBq/ml concentration, while the remaining spheres were kept cold. Additionally, the phantom included a 5 cm cylindrical cold lung-equivalent region.
To introduce outside-FOV scatter contamination, a syringe (volume 100 ml) filled with 73.71 kBq/ml of ^{18}F was fixed inside a PMMA phantom, which was positioned adjacent to the NEMA phantom. The PMMA phantom has an elliptical base, with a cross-section nearly the same size as that of the NEMA phantom. The scan acquired a total of 1.4×10^9 prompt counts over a 45-minute duration, with a corresponding random fraction of 30.7%. To evaluate scatter estimation under realistic count conditions (whole-body static PET scan), the first 2 minutes of the scan were analyzed separately, with prompt counts totaling 7.4×10^7. The estimated scatter distribution from this short scan duration was then scaled to the full scan time.

3. Results

3.1. Local/Global P_0:

Fig. 6A shows normalized local energy spectra of unscattered single photons for each incidence-angle segment defined in Fig. 2C, derived from the line-source acquisition (Section 2.6.9). Fig. 6C shows the corresponding spectra from the attenuation-free GATE experiment (Section 2.6.2, item (ii)), plotted for segment indices 0–10 (solid lines), together with the spectrum from the point-source GATE simulation (Section 2.6.2, item (i)) as a global P_0 reference (dashed line). The global P_0 closely matches the low-incidence-angle local spectra in the GATE experiment. Across both datasets, a consistent ordering with incidence angle is observed (higher segment indices correspond to higher incidence angles). However, the detailed spectral shapes of local P_0 differ between the real and simulated data, likely due to simplified detector modeling in

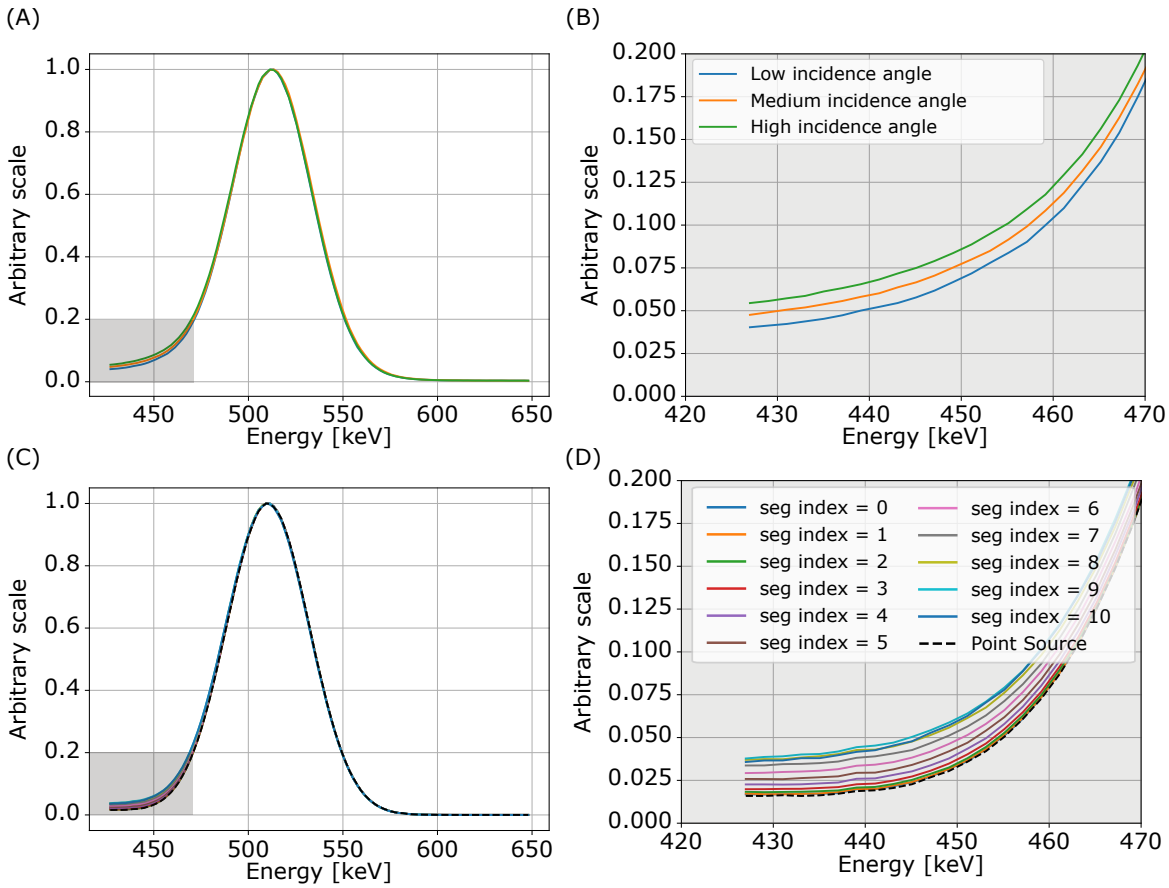

Figure 6: (A) Normalized energy spectra of unscattered single photons from a line-source acquisition on the GE SIGNA PET/MR (Section 2.6.9); incidence angles were grouped into three regions (low/medium/high) using the segmentation in Fig. 2C. (B) Zoom of the low-energy tails for (A). (C) Normalized energy spectra of unscattered single photons from the GATE simulation (Section 2.6.2, item (ii)). Only segment indices 0–10 (of the 13 defined in Fig. 2B) are shown as solid lines; the dashed line represents the spectrum from the point-source GATE simulation (Section 2.6.2, item (i)). (D) Zoom of the low-energy tails for (C). All spectra are normalized to the maximum for the tail shape comparison.

GATE (e.g., scintillation light production/transport and SiPM response). To avoid model–data mismatch, EBSE was evaluated with local P_0 derived from the same acquisition type—GATE for simulations and GE SIGNA PET/MR for real data.

3.2. Simulation of custom elliptical phantom:

Results from the simulation study (Section 2.6.4) are summarized in Figs. 7–9 as box plots, showing the distributions across seven independent noise realizations. In each subsection, a single hyperparameter is varied; the optimal value is selected from these results and then held fixed for the analyses in the subsequent subsection.

3.2.1. Energy bin width: Rebinning the 2D energy histogram has a significant impact on the computational efficiency of the optimization process. To evaluate its impact, six different energy bin widths were tested: 2, 4, 8, 14, 28, and 56 keV. Increasing the bin width progressively reduced the dimensionality of the 2D energy histogram, with its size decreasing from 112x112 to 56x56, 28x28, 16x16, 8x8, and 4x4, respectively. To ensure consistency, the energy spectra of the basis functions Fig. 3(C) and the measured data Fig. 6 were binned using the same energy bin width. Binning was performed by summing the values of adjacent high-resolution bins into a single lower-resolution bin. Among the configurations tested on GATE simulated emission data shown in Fig. 7 (A), a bin width of 28 keV was selected for subsequent analyses as it provided an optimal trade-off between computational efficiency and accuracy.

3.2.2. Number of iterations: As an iterative estimator, NEGML requires the selection of a hyperparameter, namely, the number of iterations. It is essential to ensure that this value brings the estimation process close to convergence. To determine the minimal number of iterations required for practical convergence, six different iteration numbers were evaluated: 300, 200, 100, 50, 10, and 5. These evaluations were performed after 1D weighted least squares initialization of the coefficients. Our results indicate that the minimum number of iterations required for convergence in GATE simulated emission data is conservatively estimated to be 50 iterations when using our initialization, as shown in Fig. 7 (B). The global P_0 energy spectrum was used as the unscattered energy spectrum.

3.2.3. Global/Local P_0 unscattered: Fig. 8 presents the performance comparison between activity reconstructions using EBSE with global and local P_0 energy spectra of unscattered single photons shown in Fig 6(C). The analysis highlights that the effect of using the local P_0 is most evident in off-center regions, specifically in hot regions 1, 3, and 5 shown in Fig. 4 (B). The estimated activity distributions are compared with the ground truth activity concentrations used in the GATE simulations to evaluate reconstruction fidelity further. This comparison shows improvement of EBSE with local P_0 in off-center regions 1, 3, and 5. In region 5, two outliers (open circles) originate from the same noise realization. In contrast, minimal differences are observed between the two methods for the central regions 2, 4, and 6 shown in Fig. 4 (B).

3.2.4. Sinogram mashing: The effect of the mashing factor on EBSE using global P_0 energy spectrum as the unscattered energy spectrum is shown in Fig. 9. As previously outlined, the mashing factor exerts a direct influence on the mean number of counts in the 2D energy histogram. While increasing the mashing factor improves count statistics, an excessively high mashing level can degrade the spatial resolution of the estimated scatter sinogram, thereby affecting scatter estimation accuracy. Based on the relative errors in both the background and hot regions quantified in the activity reconstructions,

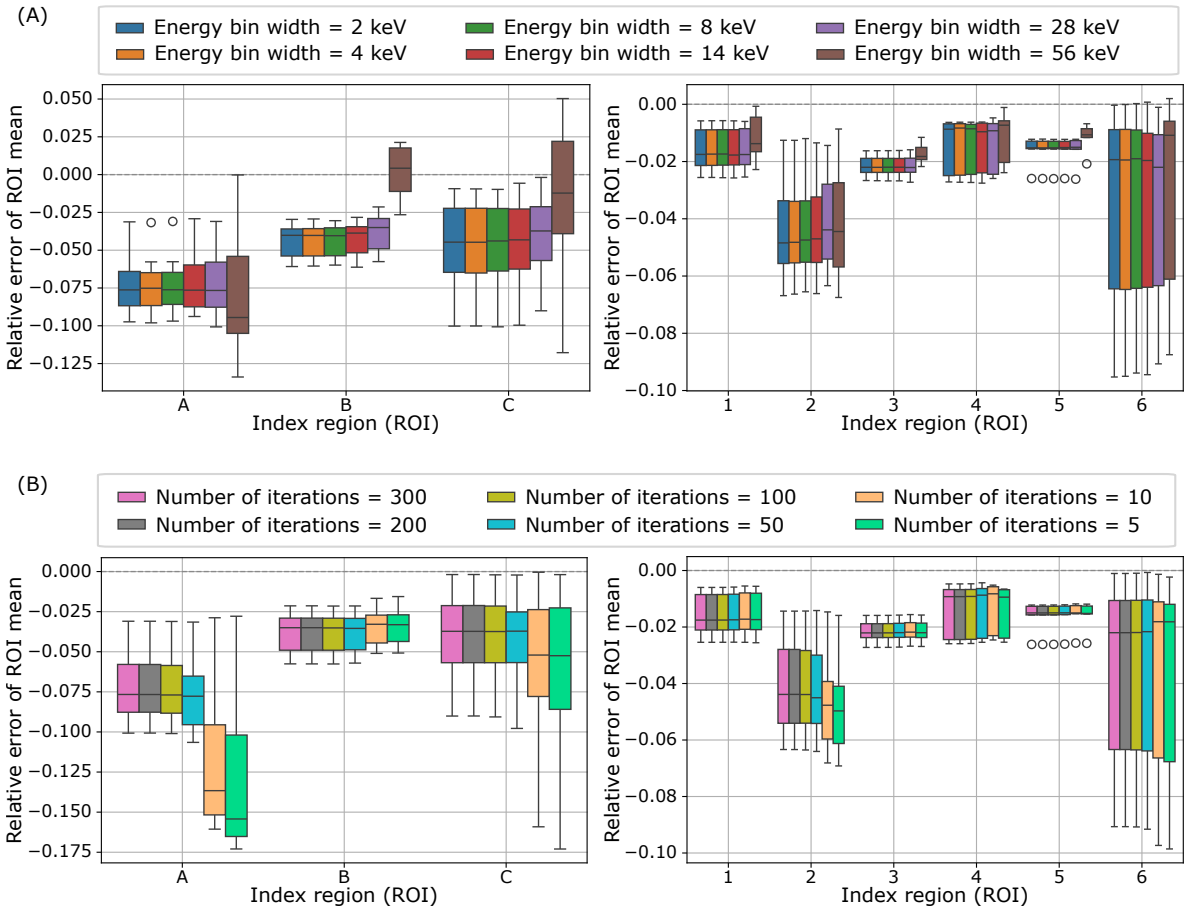

Figure 7: (A) Effect of energy binning on the reconstruction from the seven noise realizations of GATE emission data. The Y-axis represents the relative error (Eq. 6) between energy-based scatter correction reconstruction and reconstruction using only trues coincidences (GT). (B) Selection of the number of iterations for NEGML, ensuring convergence of the estimation process on GATE simulated emission data with initialization coefficients. Open circles indicate outliers from the same noise realization. The Y-axis represents the relative error (Eq. 6) between energy-based scatter correction reconstruction and reconstruction using only trues coincidences. The X-axis indices correspond to those shown in Fig. 4 (B). The global P_0 energy spectrum was used as the PDF for the unscattered energy spectrum.

the highest mashing factor yields the narrowest box plot with a median closest to zero, indicating the greatest similarity between EBSE and the ground truth.

3.3. Uniform cylinders phantom simulation

EBSE performance was evaluated using two uniform cylinders of different sizes, as described in Section 2.6.5. Fig. 10 presents results for E_{min} = 300 and 425 keV (upper bound). Panel (A) shows the small cylinder and panel (B) shows the large cylinder. For each phantom, three reconstructions are displayed. First, *Recon trues* was reconstructed

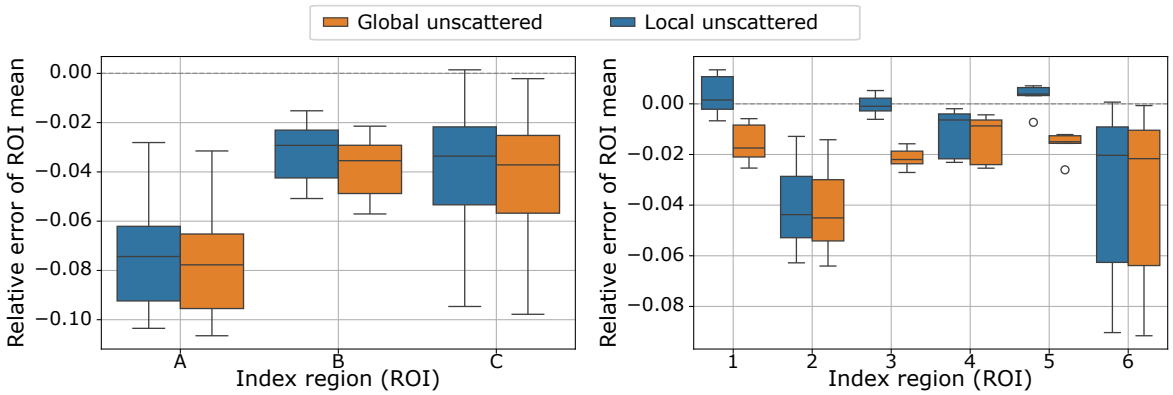

Figure 8: Performance comparison between global and local unscattered PDFs on seven noise realizations of GATE emission data. Open circles indicate outliers from the same noise realization. The Y-axis represents the relative error between energy-based scatter correction and the reconstruction using only trues coincidences. The X-axis indices correspond to those visualized in Fig. 4 (B).

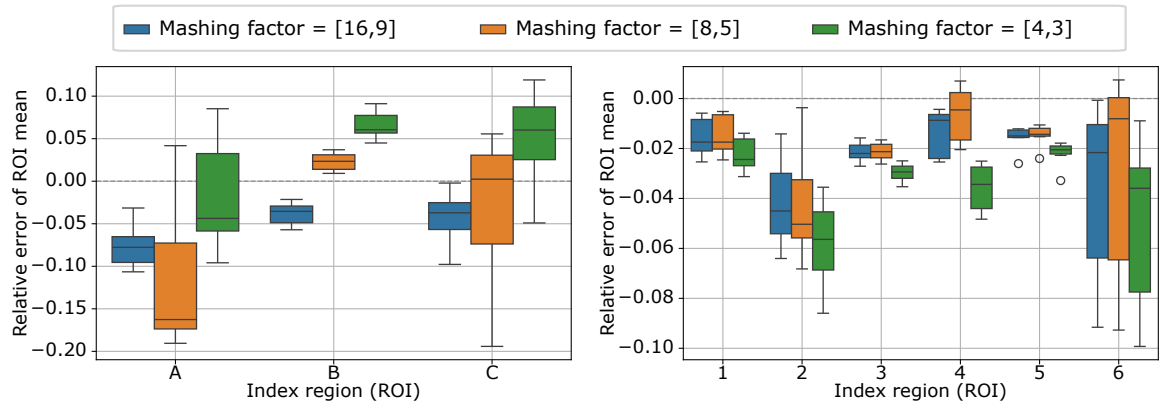

Figure 9: Impact of the mashing factor (MF) on scatter estimation. The left panel represents background regions, while the right panel corresponds to hot spheres. The Y-axis denotes the relative error between energy-based scatter correction and reconstruction using only trues coincidences. Open circles (index region 5) indicate outliers from the same noise realization. The X-axis indices correspond to those shown in Figure 4 (B). The global P_0 energy spectrum is used as the PDF for the unscattered energy spectrum.

from true coincidences only. Second and third, *EBSE_Emin300* and *EBSE_Emin425* were reconstructed using global P_0 and the basis P_1 configured with the specified $\mathrm{E_{min}}$. The post-smoothing reconstructions are shown and serve as the ground truth. The rows labeled *Err Emin* show relative-error maps (percent) with respect to ground truth. The profiles extracted along a vertical line intersect at the center of the post-smoothed reconstruction images. The y-axis reports activity concentration, and the x-axis the transaxial pixel index. Across both object sizes with uniform activity, increasing $\mathrm{E_{min}}$

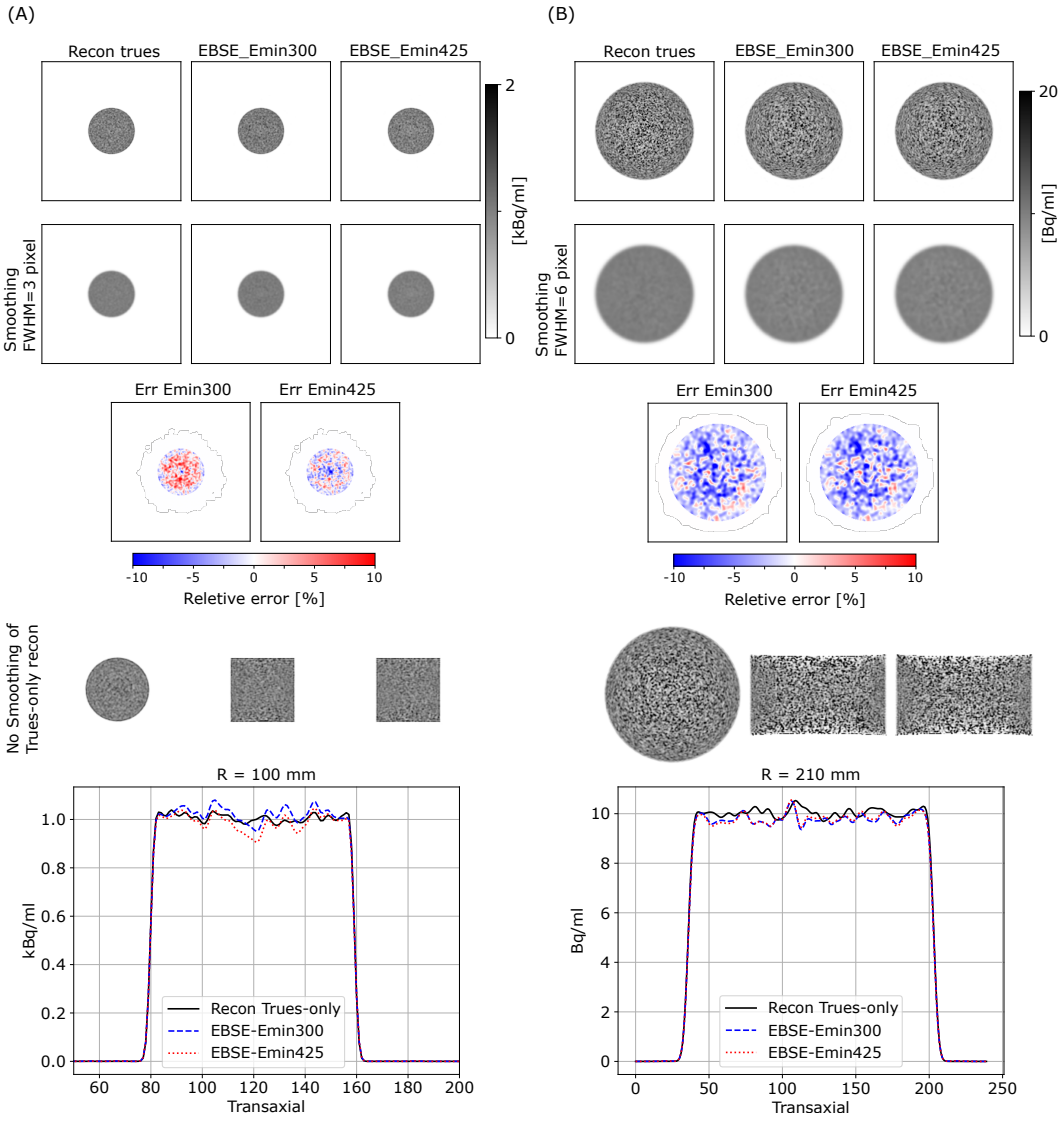

Figure 10: EBSE reconstruction results for two uniform cylinders: column (A) shows the small cylinder, and column (B) shows the large cylinder. Each column includes: *Recon trues* shows the reconstruction using only true coincidences. *EBSE_Emin300* or *EBSE_Emin425* shows the EBSE-based reconstruction and scatter correction using E_{min} equal 300 or 425 keV. The post-smoothing of each reconstruction image is also shown and serves as ground truth. *Err Emin300* or *Err Emin425* shows the relative error between the EBSE reconstruction and the ground truth. A line profile comparison between the post-smoothed EBSE and the ground truth is shown at the bottom. The y-axis represents activity concentration, and the x-axis indicates pixel index.

from 300 to 425 keV produced negligible changes in EBSE performance.

3.4. NEMA phantom with activity outside FOV simulation

To probe performance under non-uniform activity and attenuation, EBSE was further evaluated using a GATE simulation of the NEMA phantom with additional activity placed outside the FOV (Section 2.6.6). Reconstruction results are shown in Fig. 11. The image labeled *Recon trues* was reconstructed from true coincidences only and serves as the ground truth. The *no scatter corr* image was reconstructed with attenuation and randoms corrections but without scatter correction. The EBSE results (*EBSE_Emin300* and *EBSE_Emin425*) incorporate scatter correction using E_{min} = 300 and 425 keV, respectively. Line profiles extracted (bottom left) and ROI quantification for background and hot regions (bottom right) are also shown. ROIs, *background* and *hot*, were defined to exactly match the ground-truth volumes used in the simulation. Voxels with an activity concentration of 4 kBq/mL were assigned to the *background* ROI, and voxels with 16 kBq/mL to the *hot* ROI. Relative to *no scatter corr*, both EBSE reconstructions markedly reduce background uplift and restore contrast toward the ground truth, and increasing E_{min} from 300 to 425 keV yields negligible additional change. Discrepancies between the measured ROI means and the *True value* bars persist even for *Recon trues*; these are attributable to partial-volume effects.

3.5. ^{18}F-FE-PE2I and ^{18}F-SynVesT-1 simulation

To probe performance under non-uniform and spatially localized activity, EBSE was evaluated on GATE simulations of two brain tracers, ^{18}F-FE-PE2I and ^{18}F-SynVesT-1 (Section 2.6.7); results are shown in Figs. 12 and 13. The panels labeled *True activity map* and *Attenuation map* depict the activity distributions and attenuation media used in the simulations. Reconstructions from true coincidences only (*Recon trues*) serve as the imaging ground truth. EBSE reconstructions are shown for E_{min} = 300 keV (*EBSE_Emin300*) and E_{min} = 425 keV (*EBSE_Emin425*). Relative-error maps (%) with respect to *Recon trues* are provided for both EBSE settings (*Err Emin300* and *Err Emin425*). ROI means were computed using segmentations derived from the *True activity map* to match the exact simulated volumes; bar plots summarize quantification across representative regions. Relative-error maps and regional quantification both indicate that increasing E_{min} from 300 to 425 keV yields consistent improvement in EBSE performance, with reduced residual bias in high-uptake structures and background. Discrepancies between the measured ROI means and the *True value* bars persist even for *Recon trues* and are attributable to partial-volume effects.

3.6. High-counts ^{18}F-FE-PE2I simulation

To further investigate the poorer performance of EBSE with E_{min} = 300 keV, a high-count MCGPU simulation was performed using the ^{18}F-FE-PE2I activity and attenuation distributions (Section 2.6.8). After mashing with factor 16 × 9, the energy spectra of single scattered photons were analyzed as summarized in Fig. 14. Panel (A)

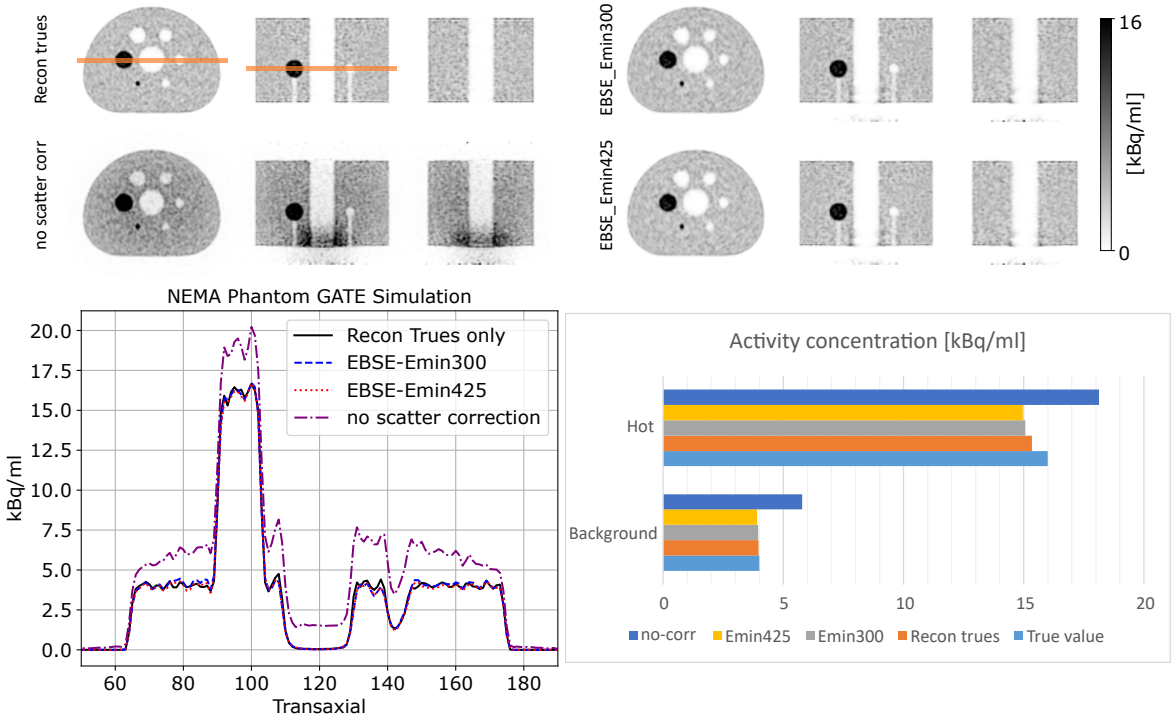

Figure 11: Performance of EBSE on GATE simulation of the NEMA phantom with activity outside the FOV (Section 2.6.6). Images show the reconstruction from the emission data: *Recon trues* reconstruction using only true coincidences (ground truth), *no scatter corr* shows the reconstruction with attenuation and random correction but without scatter correction, and *Recon EBSE* shows the EBSE-based reconstruction with scatter correction using two E_{min} equal 300 or 425 keV. Line profiles corresponding to the reconstructions. Quantification of background and hot regions in the phantom is shown in the barplot. *True value* in barplot legend represents of exact concentration used during the GATE simulation.

illustrates the three orthogonal investigations: variation across views, across TOF bins, and across radial bins. Panel (B) shows spectra for the central TOF bin and central radial bin across multiple views (*view investigation*); the curves are highly similar, indicating minimal view dependence under this selection. However, the shape of the energy spectrum is steeper than P_1 using $E_{min} = 300$ keV. Panel (C) fixes the view (vertical) and central radial bin while varying the TOF bin (*TOF investigation*); a similar shape but negligible difference is observed between TOF bins sampling inside versus outside the object. In addition, outer TOF bins have more noise in comparison to inner TOF bins. Panels (D) and (E) vary the radial bin at fixed view (vertical) and central TOF (*radial investigation*). For radial bins intersecting the brain (D), the spectra are broadly similar with gradual shape changes, whereas for radial bins outside the brain (E) the distributions are shifted toward lower energies and fall off rapidly above the photopeak. We verified that all the single-scatter energy spectra in panels

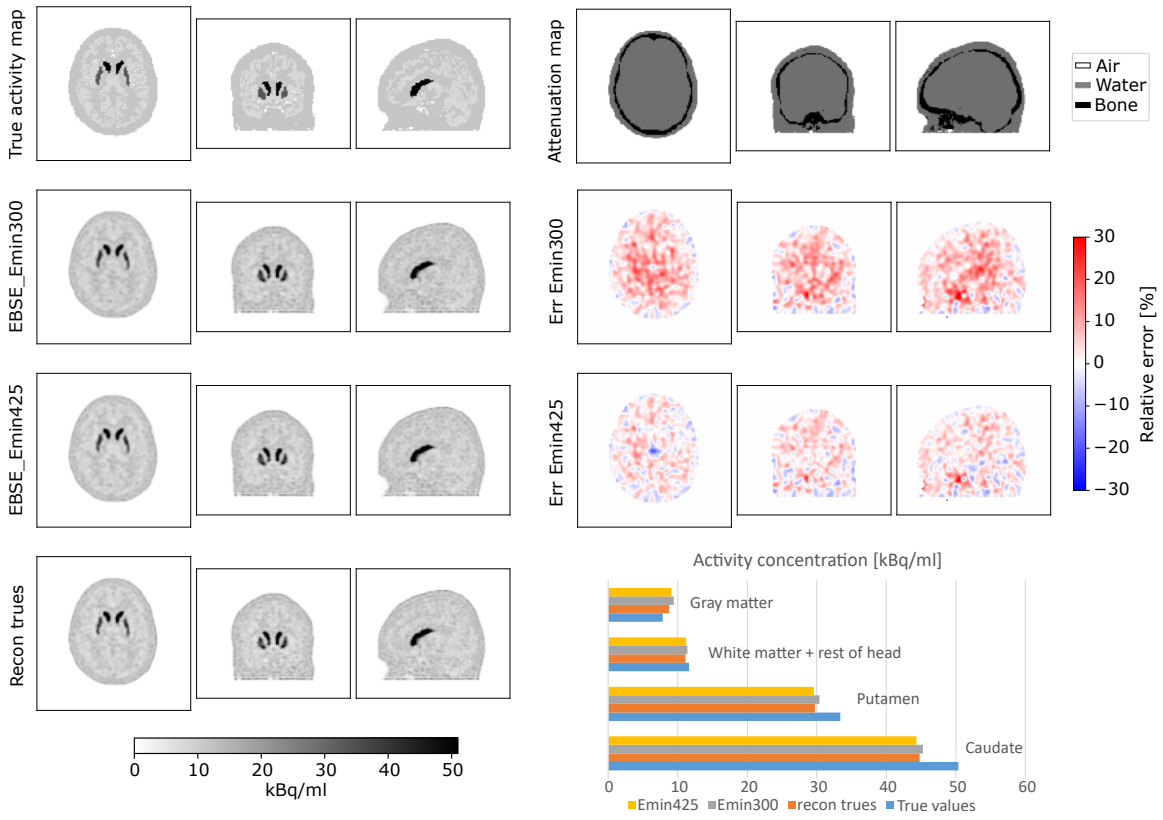

Figure 12: *True activity map* and *Attenuation map* are simulation inputs for ^{18}F-FE-PE2I simulation; *Recon Trues* is the true-only reconstruction (ground truth); *EBSE Emin300* and *EBSE Emin425* are EBSE reconstructions with E_{min} = 300 and 425 keV; *Err Emin300* and *Err Emin425* are relative-error maps with respect to *Recon Trues*; the bar plot compares region-wise mean activity for segmented based on *True activity map*. The concentration unit is kBq/ml, and the relative error is a percentage.

(B), (C) and (D) of Fig. 14 can be well represented with our model, provided that E_{min} is set to 425 keV (results not shown). However, this is not the case for the spectra of panel (E).

3.7. Acquisition NEMA phantom with activity outside FOV

The reconstruction image of EBSE on real data Section 2.6.10 is shown in Figure 15 (A and B), which presents a comparison between the tail-fitted SSS, and the EBSE method applied to NEMA phantom measurements. The experiment is conducted using a mashing factor of [16,9] and E_{min} = 300 keV. The results indicate that the EBSE correction approach does not introduce artifacts, even when scattered radiation originates from activity outside the FOV. A quantitative comparison between the two approaches is provided in Figure 16.

The plots shown in Figure 16 (A) are line profiles intersecting the cavity, comparing the local and global P_0 unscattered PDFs and E_{min} = 300 keV. The findings indicate

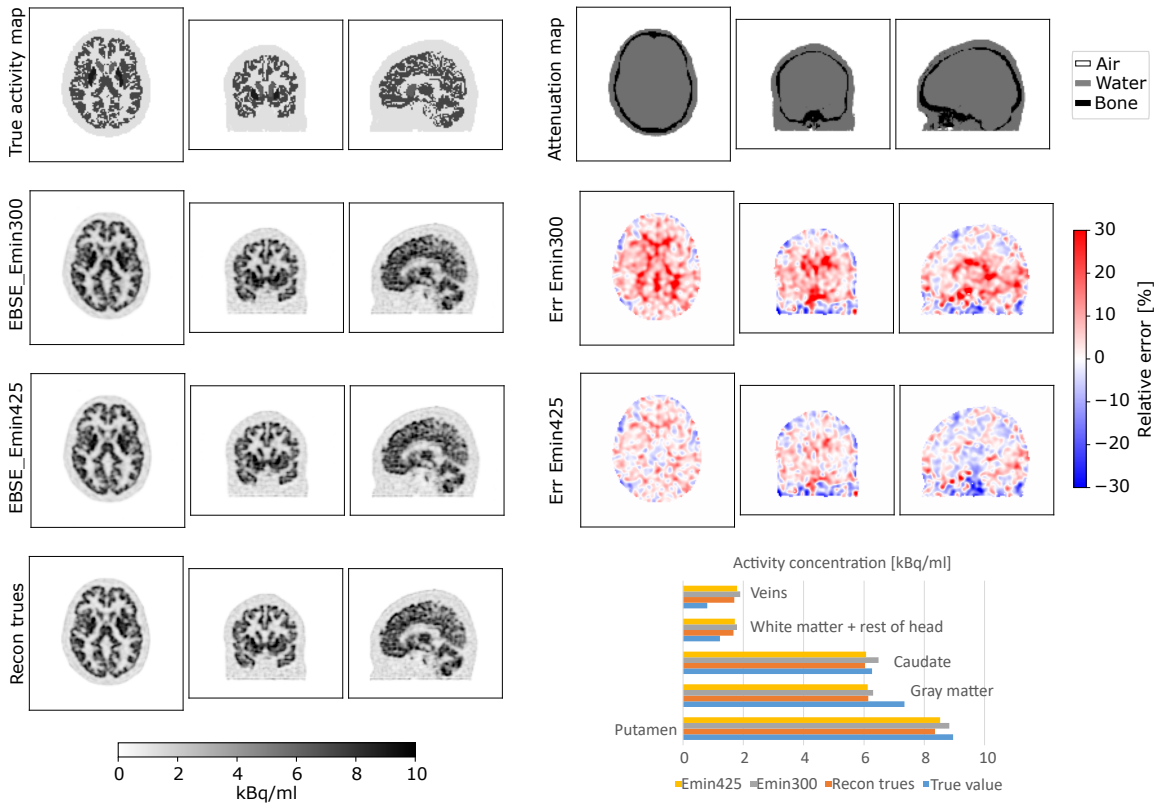

Figure 13: *True activity map* and *Attenuation map* are simulation inputs for ^{18}F-SynVesT-1 simulation; *Recon Trues* is the true-only reconstruction (ground truth); *EBSE Emin300* and *EBSE Emin425* are EBSE reconstructions with E_{min} = 300 and 425 keV; *Err Emin300* and *Err Emin425* are relative-error maps with respect to *Recon Trues*; the bar plot compares region-wise mean activity for segmented based on *True activity map*. The concentration unit is kBq/ml, and the relative error is a percentage.

that EBSE improves quantification when activity extends beyond the FOV. There is no difference between using the global and local P_0 unscattered PDF in the cavity, because the cavity is in the center, and the lowest incidence angle unscattered PDF of local P_0 shown in Fig. 6(A) is used as the global unscattered PDF. Additionally, the EBSE provided more accurate scatter estimation within the cavity compared to SSS with tail fitting, in regions adjacent to activity outside the FOV, while achieving nearly identical performance in regions distant from the external activity. Figure 16 (B) (right plot) shows the line profile intersecting the hot region, where the horizontal dashed line represents the ground truth activity, derived from the measured activity before injection into the phantom. The results confirm that the EBSE remains reliable for both hot and cold regions, exhibiting minimal influence from activity outside the FOV.

In the final stage, the effect of increasing E_{min} from 300 to 425 keV was evaluated (Fig. 17). Line profiles comparing EBSE with the ground truth concentration in background and the tail-fitted SSS show that raising E_{min} to 425 keV leads to systematic

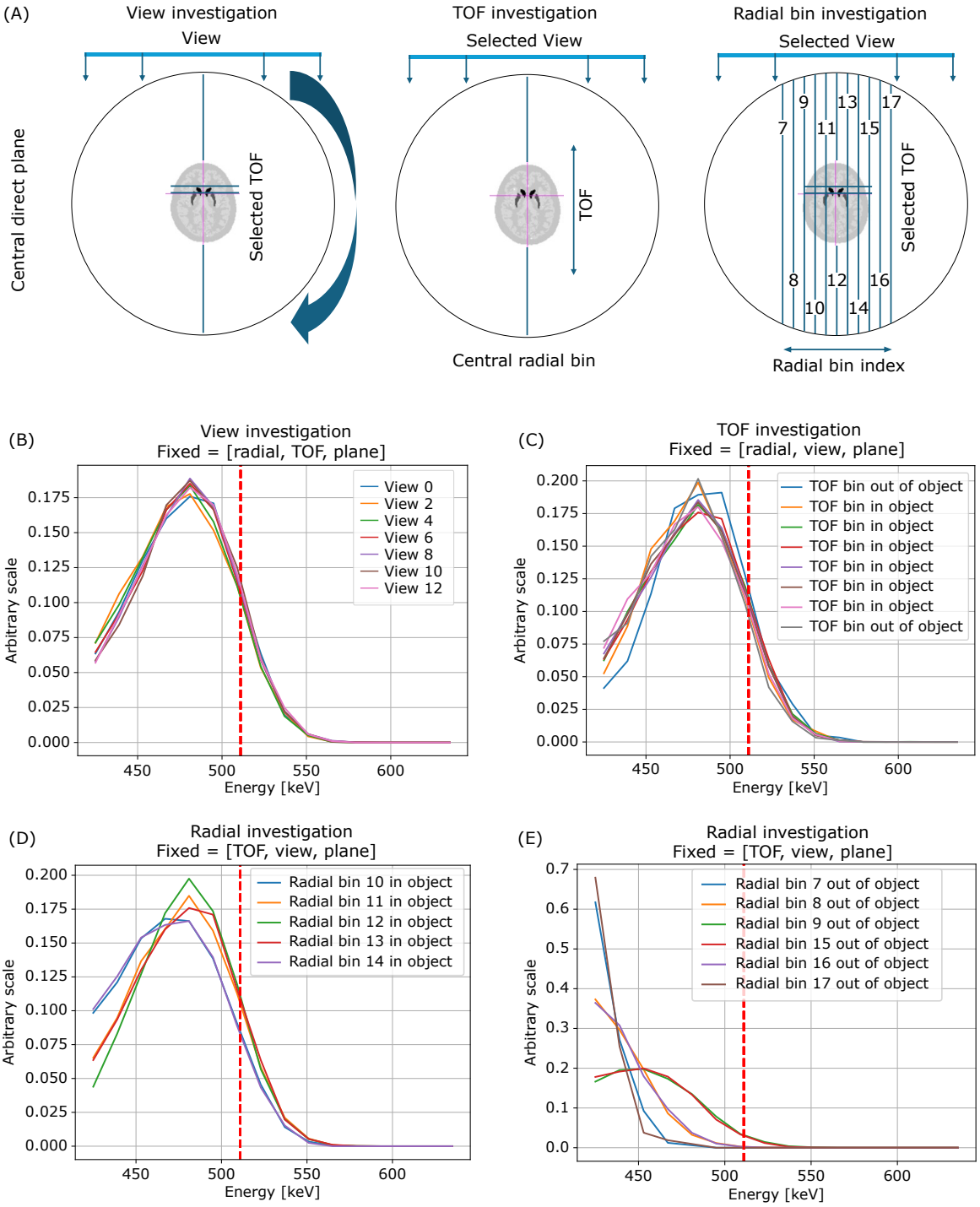

Figure 14: High-count ^{18}F-FE-PE2I Monte Carlo. Panel A illustrates the binning strategy used to extract single-scatter energy spectra. In the view investigation (panel B), the radial, TOF, and plane bins are fixed and each curve corresponds to a different view. In the TOF investigation (panel C), the radial, view, and plane bins are fixed and each curve corresponds to a different TOF bin. In the radial-bin investigation, the TOF, view, and plane bins are fixed: panel D shows radial bins inside the object and panel E shows radial bins outside the object. The vertical red dashed line marks 511 keV.

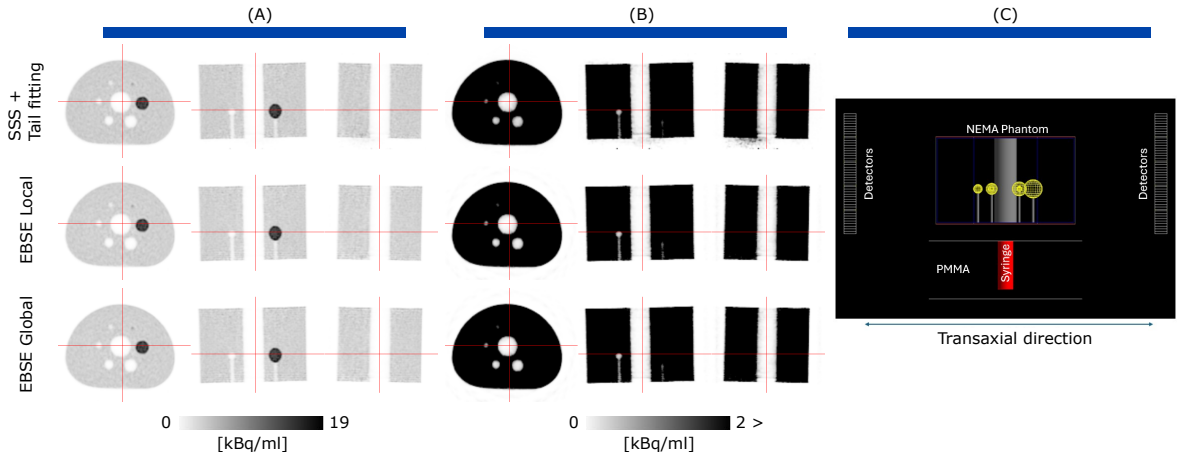

Figure 15: (A) Reconstructed activity images using scatter estimation from two different approaches. (B) Same as (A) using a compressed color scale to highlight outside FOV scatter artifacts in the tail-fitted SSS method. (C) The scheme of the NEMA phantom experiment in the GE SIGNA PET/MR scanner (top view). The comparison demonstrates that the energy-based scatter correction method more effectively mitigates artifacts caused by activity outside FOV.

overestimation of scatter, evidenced by lower reconstructed activity in background and hot region relative to ground truth.

4. Discussion

The present study evaluates an energy-based scatter estimation framework that employs three basis functions and adopts the forward model proposed by Hamill et al. 2024. The method's performance is assessed across a range of object sizes, and the sensitivity of EBSE to the position-dependent unscattered-photon energy spectrum P_0 is quantified. Moreover, increasing the upper bound on $\mathrm{E}_{\mathrm{min}}$ to model P_1 was found to enhance the generalization capability of the EBSE framework across different scenarios.

Based on a simplified analytical derivation, we developed a three-parameter model to describe the energy spectrum of single photons within the 425–650 keV window. The model expresses the spectrum as $S_0P_0 + S_1P_1 + S_2P_2$, where P_0 corresponds to the spectrum of unscattered (true) photons, and $S_1P_1 + S_1'P_2$ accounts for photons that have scattered once within the patient's body. Photons that have undergone multiple scattering events are represented by $S_2'P_2$. Consequently, the total weight for P_2 is defined as $S_2 = S_1' + S_2'$. This set of three basis functions is consistent with the model proposed by Hamill et al. 2024. Notably, in that paper, the *small-angle* and *large-angle* bases were obtained empirically from Monte Carlo simulated energy spectra along LORs inside and outside a uniform cylinder. In contrast, we obtained the shape of basis functions P_1 and P_2 analytically and determined a good value for $\mathrm{E}_{\mathrm{min}}$ by fitting our

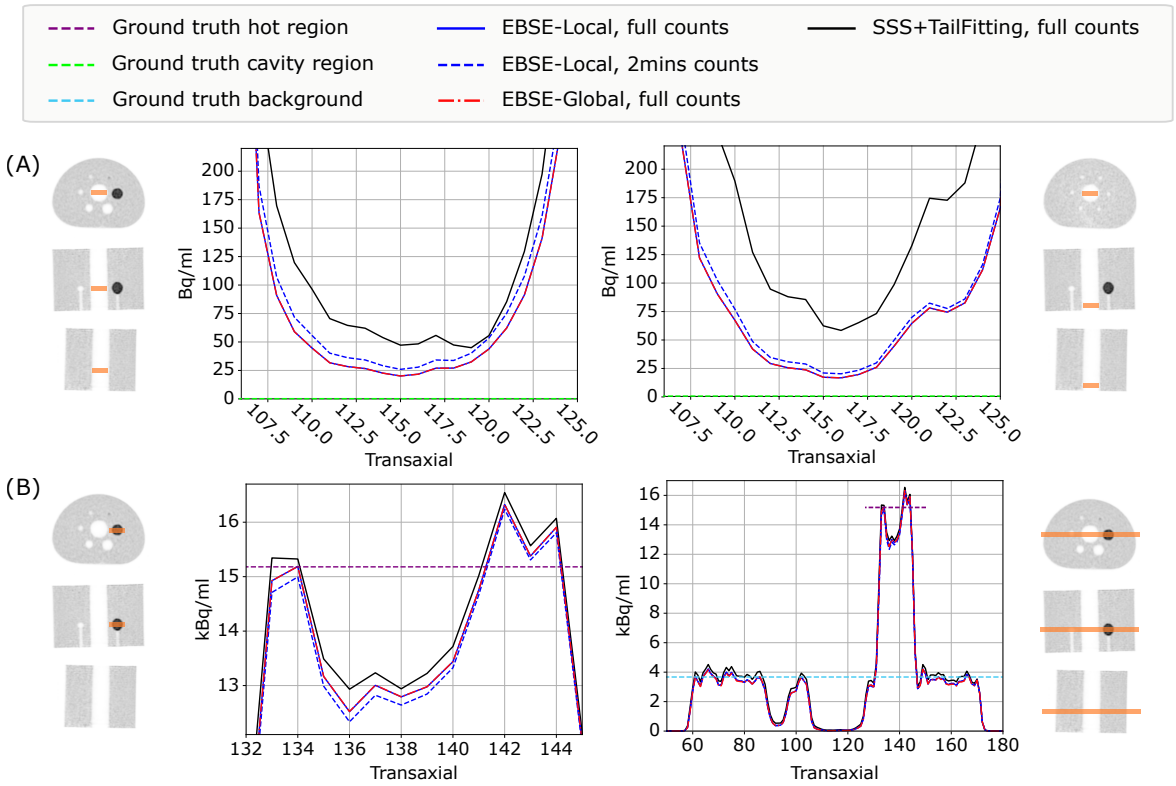

Figure 16: (A) Line profiles through the lung insert of the NEMA phantom reconstruction, comparing different scatter estimation methods across two distinct slices. The left panel corresponds to a slice located far from the activity outside FOV, while the right panel represents a slice positioned closer to the activity outside the FOV. (B) Line profiles through the hot region (37 mm diameter sphere) inserts of the NEMA phantom reconstruction are presented, with different scatter estimations being compared. The Gibbs artifacts at its boundary due to resolution modeling in the reconstruction. The right panel corresponds to a profile of the image in a transaxial direction, and the left panel represents the same profile focused on the hot region. The solid line indicates scatter estimation using 1.4×10^9 prompt counts, whereas the dashed line corresponds to estimation using only 7.4×10^7 prompt counts. The experiment is conducted using a mashing factor of [16,9].

model to the single-scatter contributions from all LORs intersecting the activity. The primary aim of fitting this model to the 2D energy histogram is to recover S_0P_0, because reliable image reconstruction depends on accurate estimation of the true coincidences. Efthimiou et al. 2022 attempted to estimate the trues fraction using a trues-only model, but this approach showed limited stability. Incorporating the scattered components S_1P_1 and S_2P_2 improves stability by constraining the estimated contribution of scattered photons. However, when P_1 is made steeper by selecting a higher $\mathrm{E_{min}}$, this constraint weakens. The original selection of $\mathrm{E_{min}} = 300$ keV was based on measurements in

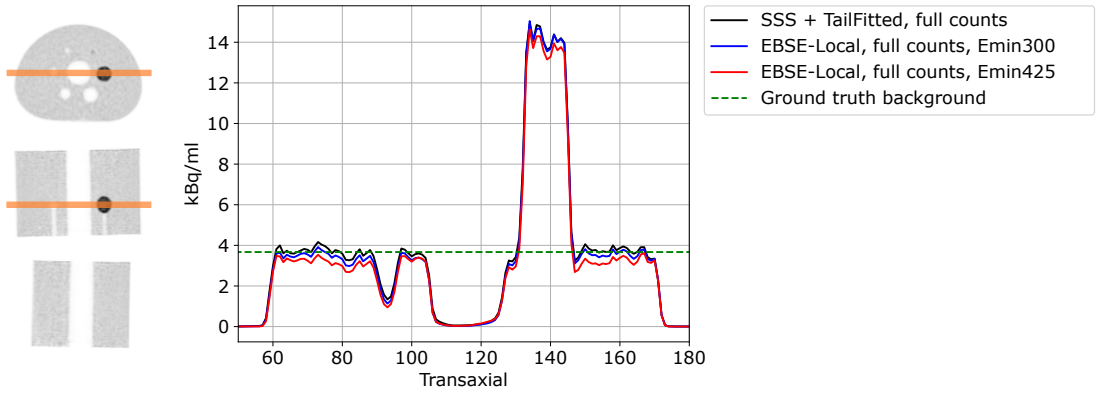

Figure 17: Line profile for the NEMA phantom acquisition with a syringe placed outside the FOV (Section 2.6.10). Curves compare the tail-fitted SSS reconstruction (black) with EBSE using local P_0 and E_{min} = 300 keV (blue) and E_{min} = 425 keV (red). The green dashed line denotes the ground-truth background activity. The y-axis shows activity concentration (kBq/mL); the x-axis is the transaxial pixel index.

a uniform 20 cm cylinder. However, our brain simulations indicate that for strongly non-uniform activity distributions, this constraint becomes too strict. Under these conditions, better performance is achieved with E_{min} = 425 keV. Notably, the single-scatter energy spectra observed along LORs that do not intersect the object (Fig. 14(E)), exhibit shapes that our current scatter bases cannot capture. This mismatch may bias EBSE estimates in non-TOF emission data, where the object reconstruction is more sensitive to the surrounding background. We will therefore investigate improvements to the model that achieve a better balance between strong constraints, which provide robustness to system modeling errors and noise, and sufficient flexibility to represent the full range of possible energy spectra.

Utilizing the NEGML optimization algorithm with initialization significantly reduces the required number of iterations, thereby accelerating the estimation process. The results in GATE simulated emission data from the hot regions indicate that the difference between using 300 iterations and as few as 50 iterations is negligible. However, using fewer than 50 iterations is not recommended in the background regions. Notably, using fewer iterations in certain regions produces wider box plots—reflecting greater instability—and shifts the median downward, indicating an overestimation of scatter. Findings reported by (Hamill et al. 2024) indicate that standard MLEM without advanced initialization required 200 iterations.

The second approach to reduce computation time involved rebinning the 2D energy histogram. Theoretically, a reasonable energy bin width can be approximated as half of the energy resolution. Based on our ^{18}F point source measurement, the GE SIGNA PET/MR scanner demonstrated an energy resolution of 11.2%. The investigation shows that for energy bin widths up to 28 keV, the variation in relative error remains small. When the bin width exceeds 28 keV, the size of the box plots increases in

some regions, indicating reduced stability in scatter estimation (see Figure 7 (A)). However, in certain regions, a slight improvement in scatter estimation accuracy was observed when using a 56 keV bin width, which cannot be explained based on energy resolution. This improvement may reflect inaccuracies in the scatter model introduced by simplifications. The 28 keV energy bin-width reduced the 2D energy histogram size from 112 x 112 to 8 x 8, which significantly reduced the computation time, making the estimator approximately 32 times faster. In our optimized setting the down-sampled scatter sinogram (mashing=[16,9]) estimation process took 12 minutes using six CPU cores (AMD EPYC 7773X, 64-Core Processor, 2.2 GHz).

The impact of incidence-angle dependence is negligible at the centre and alters the estimated activity by only approximately 2% off-centre (based on GATE simulation results; Fig. 8). This suggests that, for most applications—brain imaging in particular—a single low-incidence-angle energy spectrum (or a spectrum extracted from a point source at isocentre) is sufficient.

The observed similarity between the energy spectrum of a source at the center of the FOV and the lowest-incidence-angle segment in the GATE simulated emission data justified using the lowest-incidence-angle segment as the global energy spectrum of unscattered single photons for NEMA phantom scatter estimation. However, we think the distinction between different angle classes in the energy spectrum of unscattered photons becomes increasingly important for large axial-FOV scanners, as they are likely to detect a greater fraction of events at higher angles of incidence.

Adjusting the mashing factor influences two critical parameters: the average count per 2D energy histogram and the spatial resolution of scatter estimations. Increasing the mashing factor reduces statistical noise and accelerates computation. Results from GATE simulated emission data indicate better performance in most hot and background regions using the highest level of mashing. Notably, using the scanner sensitivity sinogram in the up-sampling process of the scatter-only sinogram is an approximation, because the scanner sensitivity is defined for true coincidences, while the sensitivity sinogram for scatter events may differ.

Overall, the recommended strategy for energy-based scatter estimation is to employ the nine-parameter model with appropriate initialization, a high level of mashing, and the use of a global energy spectrum for single unscattered photons. This strategy is applicable under the condition that a 2% error (off-centered) is considered negligible in studies involving large objects. To better represent the differing shapes of the scattered energy spectrum inside the object, selecting E_{min} from the upper end of the tested range is advisable, provided that the PET system matrix and the shape estimation of the random energy spectrum used during the reconstruction are sufficiently accurate.

Tail-fitted single-scatter simulation and energy-based scatter estimation represent complementary methodologies, each with advantages and limitations. At present, no definitive consensus exists regarding their superiority; selection should be informed by the specific requirements and constraints of the imaging task. A combination of the two approaches may offer the most effective means of leveraging both prior knowledge and

information contained in the data.

5. Conclusion

Energy-based scatter estimation reduced out-of-FOV scatter artifacts compared with single-scatter simulation with tail fitting, and performed at least as well as vendor SSS elsewhere. The approach remains usable when no attenuation map is available (e.g., joint attenuation–activity reconstruction (Rezaei et al. 2019)). Computational cost was lowered by using NEGML with improved initialization and by down-sampling the 2D energy histogram, with minimal loss in accuracy. Accounting for the incidence angle in the unscattered spectrum provided a small benefit in off-central FOV regions.

EBSE performance on brain-sized objects suggests that a steeper P_1 function is necessary at $E_{min} = 425$ keV. For the GATE simulations, increasing E_{min} improved the performance on the brain images, without degrading the performance on the (more uniform) phantoms. However, for the measured data, an overestimation was observed when E_{min} was increased. We believe this is not due to a fundamental problem of the approach, but to data inconsistencies in the measured data, which should be remedied by improving the model of the acquisition process. This suggests that with the current basis functions, ESBE is very sensitive to such modeling errors.

Future work will include: (i) improving the basis functions to model limited-angle, out-of-object scatter; (ii) dealing correctly with ^{176}Lu and Compton scatter recovery, to facilitate evaluation of the method on real data.

Acknowledgments

We would like to express our sincere thanks to everyone who contributed to the success of this study. In particular, we are grateful to Timothy Deller for providing insightful discussions throughout this research. In addition, we are grateful to the anonymous reviewers, whose comments inspired us to investigate the accuracy of our approach for the challenging ^{18}F-FE-PE2I and ^{18}F-SynVesT-1 TOF-PET brain scans. This work was supported in part by the Research Foundation—Flanders (FWO) under grant G062220N. The Department of Imaging and Pathology at KU Leuven received funding from GE HealthCare for this research project.

Appendix A. Analytical model for the scatter energy spectrum

The (single photon) scattered energy spectrum is modeled as a combination of single scattered and multiple scattered.

A.1. Single Compton scattered energy spectrum (P_1)

The fraction of the energy that is transferred from the incoming photon (at 511 keV) to the scattered photon is given by Compton's equation:

$$f(E_0,\theta) = \frac{E}{E_0} = \frac{1}{1+\frac{E_0}{m_e c^2}(1-\cos\theta)}. \tag{A.1}$$

where E_0 is the energy of the incoming photon, E the energy of the scattered photon, θ the scattering angle and $m_e c^2 = 511$ keV. This equation can be reorganized to compute the angle from the energies of the incoming and scattered photons:

$$\theta(E_0,E) = \arccos\left(1 - \frac{m_e c^2}{E_0}\left(\frac{E_0}{E} - 1\right)\right) \tag{A.2}$$

The single scattered energy spectrum we wish to compute corresponds to the derivative of the scatter cross-section with respect to the energy and can be computed as:

$$\begin{aligned}\text{SingleScatteredSpectrum}(E_0,E) &= \frac{\mathrm{d}\sigma}{\mathrm{d}E}(E_0,E) \\ &= \frac{\mathrm{d}\sigma}{\mathrm{d}\Omega}(E_0,\theta)\,\frac{\mathrm{d}\Omega(\theta)}{\mathrm{d}\theta}\left|\frac{\mathrm{d}\theta(E_0,E)}{\mathrm{d}E}\right|.\end{aligned} \tag{A.3}$$

The differential cross section for single scattering with angle θ is given by the Klein-Nishina formula:

$$\frac{d\sigma}{d\Omega}(E_0,\theta) = K(E_0,\theta) = \frac{1}{2} r_e f^2(E_0,\theta)\left(f(E_0,\theta) + \frac{1}{f(E_0,\theta)} - \sin^2\theta\right) \tag{A.4}$$

where r_e is the classical electron radius, which can be ignored here, because we are only interested in the shape of the energy spectrum.
The solid angle $d\Omega(\theta)$ covered by all scattered directions with angle θ is the area of a circular strip with radius $\sin\theta$ and width $d\theta$. Consequently

$$\frac{d\Omega(\theta)}{d\theta} = 2\pi\sin\theta \tag{A.5}$$

The derivative of the angle $\theta(E_0,E)$ with respect to E equals

$$\begin{aligned}\frac{\mathrm{d}\theta(E_0,E)}{\mathrm{d}E} &= \frac{\mathrm{d}}{\mathrm{d}E}\arccos\left(1 - \frac{m_e c^2}{E_0}\left(\frac{E_0}{E} - 1\right)\right) \\ &= -\frac{(m_e c^2)/E^2}{\sqrt{1-\left(1+\frac{m_e c^2}{E_0} - \frac{m_e c^2}{E}\right)^2}}.\end{aligned} \tag{A.6}$$

Inserting these three derivatives into equation (A.3) produces the energy spectrum of the single scattered photons in PET, which is shown as the black curve in Figure 3:

$$\begin{aligned}\text{EnergySpectrum}(E_0, E) = \pi\, f^2(E_0,\theta) \\ \times \left(f(E_0,\theta) + f(E_0,\theta)^{-1} - \sin^2\theta\right) \\ \times \frac{m_e c^2}{E^2}\,\sin\theta \\ \times \frac{1}{\sqrt{1-\left(1+\frac{m_e c^2}{E_0}-\frac{m_e c^2}{E}\right)^2}}.\end{aligned} \tag{A.7}$$

For application to PET, we set E_0=511 keV. To simplify the model for application in an energy window near 511 keV, we use a linear approximation, i.e. the line tangent to EnergySpectrum(E_0, E) at E=E_0 = 511 keV. Somewhat lengthy calculations (without approximations) produce

$$\lim_{E\to E_0}\frac{d}{dE}\,\text{SingleScatteredSpectrum}(E_0, E) = \frac{1}{E_0} \tag{A.8}$$

Consequently, the linear approximation is drawn from the origin $(0, 0)$ to the rightmost point of the spectrum at $E = 511\,\text{keV}$, i.e., $(511, \text{EnergySpectrum}(511, 510))$, shown as the red dashed line in Fig. 3. This approximation is based on the pure Klein–Nishina (KN) spectrum and does not include attenuation. Empirically, single-scatter spectra are steeper than the pure KN prediction. To account for this, a steeper linear basis function is defined, which intersects the x-axis at $E_{min} > 0$; the case $E_{\text{min}} = 300\,\text{keV}$ is illustrated by the red dotted line in Fig 3.

A.2. Double-Compton scattered energy spectrum (P_2)

In the energy window around 511 keV, the multiple scatters are dominated by double-Compton scattered photons. An approximation of the double-scattered energy spectrum can be obtained by convolving the single-scattered spectrum equation (A.7) with itself. The computation is further simplified by convolving the linear approximation with itself. Writing this linear approximation as aE, with a the slope and E the energy, one obtains for the double-scattered energy spectrum:

$$\begin{aligned}\text{DoubleScatteredSpectrum}(E_0, E) \simeq a^2\,(E_0 - E) \\ \times \left(E_0 E + \frac{(E_0 - E)^2}{6}\right).\end{aligned} \tag{A.9}$$

As a first-order approximation near E_0 only the first-order term is kept: $\text{DoubleScatteredSpectrum}(E_0, E) \simeq a^2\Big(E_0^2\,(E_0 - E)\Big)$. This linear approximation is shown in Figure 3 (A) as the purple dashed line. The figure also shows plots of the (numerical) convolution of the single scattered spectrum with itself (blue), and the (analytical) convolution of the linearized single scattered spectrum with itself (yellow dash-line). In this work, a weighted sum of the linearized single and double energy scatter spectra, convolved with the Gaussian energy resolution, was used Figure 3 (C).

A.3. Accounting for attenuation and solid angle

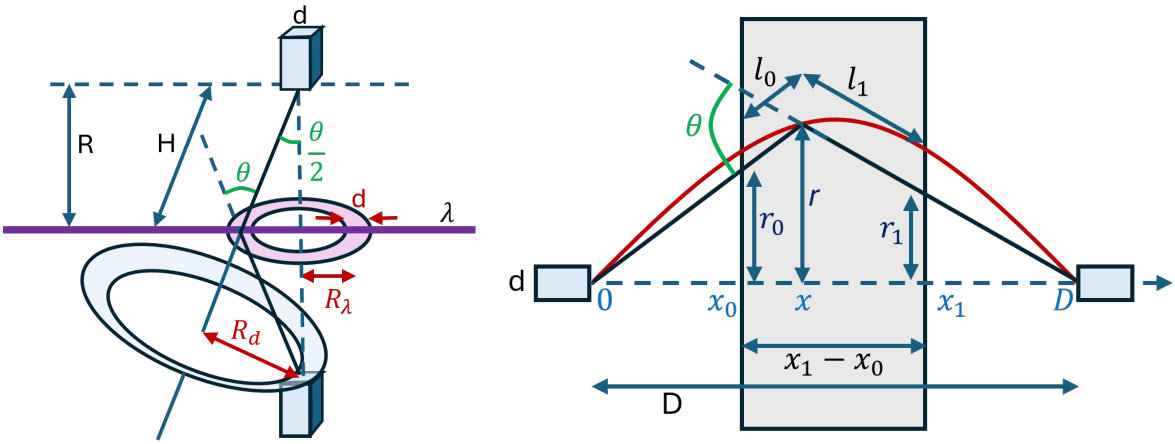

(a) (b)

Figure A1: Left, solid angle: the two detectors obtain scattered coincidences from the pink ring in the uniform phantom; when one photon reaches the top detector, the other photon is emittted to the blue ring. Right, attenuation: the locus of all possible scatter points is shown in red; the attenuation effect is computed by averaging over all possible broken lines.

The equation for the single scattered photons derived above only computes the spectrum of the scattered photon at a particular scatter point, ignoring the effects of the attenuation and the solid angle associated with the PET detectors. Here, the model is updated to predict the single scatter photon spectrum, for the case of two PET detectors, imaging a uniform bar phantom that has a particular thickness along the LOR, and is very large in the other two dimenstions, and positioned at equal distance from both detectors. The setup is illustrated in figure A1.

First, assume that the bar phantom is very thin, and consider a particular scatter angle θ (fig. A1(a)). To reach the detectors, the photon pair must travel along a broken line with angle θ, with one of the photons scattering immediately after emission. The photons enter the detectors at an angle $\theta/2$ with the detector axis.

The fraction of (randomly emitted) unscattered photons reaching one of the detectors equals

$$f_u(\theta) = \frac{d^2 \cos(\theta/2)}{2\pi H^2} = \frac{d^2}{2\pi R^2} \cos^3 \frac{\theta}{2} \qquad \text{with} \qquad \cos \frac{\theta}{2} = \frac{R}{H}, \tag{A.10}$$

where d^2 is the area of the detector, R is the distance between the flat source and each of the detectors, and H is the distance between the scatter point and each of the detectors. The set of scatter points from which the detector can be reached is the intersection of the phantom with all possible broken lines (with angle θ) connecting the detectors. This intersection is a ring with radius $R_\lambda = R \tan(\theta/2)$ and width d, shown in figure A1(b), which has an area $\Lambda(\theta) = 2\pi R \tan(\theta/2) d$.

If the unscattered photon reaches the detector, then the scattered photon will be sent towards a ring with radius $R_d = 2R\sin(\theta/2)$ and width d, chosen such that the other detector touches this ring (see figure A1(a)). Its area equals $S_d(\theta) = 2\pi R\sin(\theta/2)d$. Combining the three factors given above produces the probability that a photon pair, of which one photon scattered at an angle θ, is detected by the detector pair:

$$\text{sens}_\text{d} = f_u(\theta)\frac{\Lambda(\theta)}{S_d(\theta)} = \frac{d^2}{4\pi R^2}\cos^2\frac{\theta}{2}. \tag{A.11}$$

Now, this result is extended to a uniform bar phantom with finite thickness, as illustrated in figure A1(b). Consider two opposing detectors with one detector at $x = 0$ and the other at $x = D$. Between the detectors is the uniform phantom, its intersection with the LOR extends from x_0 to x_1. To compute the attenuation, an integration along all scatter points in the object will be carried out. Straightforward calculations reveal that the locus of the scatter points is given by

$$r(x,\theta,D) = \frac{-D + \sqrt{D^2 + 4\tan^2\theta(D-x)x}}{2\tan\theta} \tag{A.12}$$

where $r(x,\theta,D)$ is the distance between the scatter point and the LOR between the two detectors, see figure A1(b). For every point (x,r), we consider first the case where the scattered photon (with energy after scattering E_θ) travels to the detector at $x = 0$. The annihilation point must then be located on the right part of the broken line, which has an intersection length l_1 with the phantom. When traveling along this line, the photon pair faced an attenuation $\exp(-\mu_0 l_1)$, where μ_0 is the attenuation of water at 511 keV. When traveling along the other part of the broken line, the scattered photon faced an attenuation $\exp(-\mu_\theta l_0)$, with l_0 the traveling length in the phantom and μ_θ the attenuation of water at the energy E_θ. The calculation for the case when the scattered photon travels to the other detector is identical because of the symmetry. Consequently, the sensitivity loss due to solid angle and attenuation effects equals

$$\text{sensit}(\theta,D) = \cos^2\frac{\theta}{2}\frac{1}{(x_1-x_0)^2}\int_{x_0}^{x_1}((x-x_0)e^{-\mu_0 l_0-\mu_\theta l_1} + (x_1-x)e^{-\mu_\theta l_0-\mu_0 l_1})dx \tag{A.13}$$

where we omitted the argument (x,θ,D) of l_0 and l_1, we multiplied the integral with (A.11) and normalized to the case without attenuation and with forward scatter ($\theta = 0$). The Klein-Nishina scatter line with slope given by equation (A.8) intersects the energy axis at $E_\text{min} = 0$ keV. After multiplying this line with the sensitivity (A.13) for a PET diameter $D = 100$ cm and a uniform phantom thickness of 20 cm, the resulting curve is still well approximated with a line (for energies above 425 keV), but its higher slope increases E_min to 283 keV. This result agrees well with $E_\text{min} \simeq 300$ keV as obtained with Monte Carlo simulations. When the thickness of the phantom is varied from 10 to 40 cm, E_min varies from 239 keV to 334 keV.

References

Bendriem, B., R. Trebossen, V. Frouin, and A. Syrota (1993). "A PET scatter correction using simultaneous acquisitions with low and high lower energy thresholds". *1993 IEEE Conference Record Nuclear Science Symposium and Medical Imaging Conference*, 1779–1783 vol.3.

Collins, D., A. Zijdenbos, V. Kollokian, J. Sled, N. Kabani, C. Holmes, and A. Evans (1998). "Design and construction of a realistic digital brain phantom". *IEEE Transactions on Medical Imaging* 17.3, pp. 463–468.

Dikaios, N., T. J. Spinks, K. Nikita, and K. Thielemans (2006). "Double Scatter Simulation using the Polarized Klein-Nishina formula". 4, pp. 2146–2150.

Efthimiou, N., J. S. Karp, and S. Surti (May 2022). "Data-driven, energy-based method for estimation of scattered events in positron emission tomography". *Physics in Medicine and Biology* 67 (9), p. 095010.

Grootoonk, S, T. J. Spinks, D Sashin, N. M. Spyrou, and T Jones (Dec. 1996). "Correction for scatter in 3D brain PET using a dual energy window method". *Physics in Medicine and Biology* 41 (12), pp. 2757–2774.

Hamill, J. J., J. Cabello, S. Surti, and J. S. Karp (Jan. 2024). "Energy-based scatter estimation in clinical PET". *Medical Physics* 51 (1), pp. 54–69.

Herraiz, J. L., A. Lopez-Montes, A. Badal, and M. Carlo (2024). "Computer Programs in Physics MCGPU-PET: An open-source real-time Monte Carlo PET simulator". *COMPUT PHYS COMMUN* 296, p. 109008.

Jan, S et al. (Oct. 2004). "GATE: a simulation toolkit for PET and SPECT". *Physics in Medicine and Biology* 49 (19), pp. 4543–4561.

Levin, C. S., S. H. Maramraju, M. M. Khalighi, T. W. Deller, G. Delso, and F. Jansen (Aug. 2016). "Design Features and Mutual Compatibility Studies of the Time-of-Flight PET Capable GE SIGNA PET/MR System". *IEEE Transactions on Medical Imaging* 35 (8), pp. 1907–1914.

Ollinger, J. M. (Jan. 1996). "Model-based scatter correction for fully 3D PET". *Physics in Medicine and Biology* 41 (1), pp. 153–176.

Popescu, L. M., R. M. Lewitt, S. Matej, and J. S. Karp (June 2006). "PET energy-based scatter estimation and image reconstruction with energy-dependent corrections". *Physics in Medicine and Biology* 51 (11), pp. 2919–2937.

Rezaei, A., G. Schramm, S. M. Willekens, G. Delso, K. V. Laere, and J. Nuyts (Nov. 2019). "A Quantitative Evaluation of Joint Activity and Attenuation Reconstruction in TOF PET/MR Brain Imaging". *Journal of Nuclear Medicine* 60 (11), pp. 1649–1655.

Shao, L., R. Freifelder, and J. Karp (1994). "Triple energy window scatter correction technique in PET". *IEEE Transactions on Medical Imaging* 13.4, pp. 641–648.

Van Slambrouck, K. and J. Nuyts (2014). "Reconstruction Scheme for Accelerated Maximum Likelihood Reconstruction: The Patchwork Structure". *IEEE Transactions on Nuclear Science* 61.1, pp. 173–181.

REFERENCES

Watson, C. (2005). "Extension of Single Scatter Simulation to Scatter Correction of Time-of-Flight PET". IEEE, pp. 2492–2496.

Watson, C. C., J. Hu, and C. Zhou (Nov. 2018). "Extension of the SSS PET scatter correction algorithm to include double scatter". IEEE, pp. 1–4.

Zaidi, H. and K. F. Koral (May 2004). "Scatter modelling and compensation in emission tomography". *European Journal of Nuclear Medicine and Molecular Imaging* 31 (5), pp. 761–782.